CPTNP-2025-026

Probing Purely Inelastic Scalar Dark Matter Across Colliders and Gravitational Wave Observatories

Jinhui Guo,[1,*] Jia Liu,[2,3,†] Chenhao Peng,[2,‡] and Xiao-Ping Wang[4,§]

[1]*School of Physics, Beihang University, Beijing 100191, China*

[2]*School of Physics and State Key Laboratory of Nuclear Physics and Technology, Peking University, Beijing 100871, China*

[3]*Center for High Energy Physics, Peking University, Beijing 100871, China*

[4]*School of Physics, Beihang University, Beijing 100083, China*

Abstract

We propose and study a purely inelastic scalar dark matter model, where two real scalars-dark matter ϕ_1 and its excited partner ϕ_2 interact with the Standard Model via a Higgs portal. After mass diagonalization, only inelastic couplings remain, allowing the model to evade stringent bounds from direct detection. We show that thermal (co-)annihilation between ϕ_1 and ϕ_2 naturally yields the observed dark matter relic abundance. The same interaction structure can induce a strongly first-order phase transition in the early universe, generating detectable gravitational waves in upcoming experiments. Meanwhile, the slight mass splitting between ϕ_1 and ϕ_2, along with the heavy off-shell mediator SM Higgs, leads to long-lived particle signatures of ϕ_2 at the HL-LHC via the displaced muon-jets technique. We pinpoint a feasible parameter space where the correct relic abundance, observable gravitational waves, and collider signals can all be achieved concurrently, presenting a valuable chance to validate this scenario through a comprehensive examination encompassing cosmological, astrophysical, and collider investigations.

* guojh23@buaa.edu.cn

† jialiu@pku.edu.cn

‡ chenhaopeng@stu.pku.edu.cn

§ hcwangxiaoping@buaa.edu.cn

CONTENTS

I. INTRODUCTION

Following the discovery of the Higgs boson at the LHC, understanding the properties of the electroweak phase transition (EWPT) has emerged as a significant challenge in modern particle physics [1, 2]. Lattice studies within the framework of the Standard Model (SM) indicate that the EWPT proceeds as a continuous crossover rather than a first-order phase transition [3–5]. However, in various theoretical frameworks beyond the SM, such as the real singlet scalar extension to the SM (xSM) [6–19], the two-Higgs-doublet model [20–30], and others, the inclusion of additional "scalars" alongside the SM Higgs field can lead to a first-order electroweak phase transition

(FOEWPT). This FOEWPT has the potential to push the early Universe out of thermal equilibrium, creating conditions conducive to electroweak baryogenesis [31–33], a process explaining the observed matter-antimatter asymmetry in the universe. Furthermore, a first-order electroweak phase transition may generate detectable gravitational waves (GWs), offering prospects for future GW observatories.

The newly introduced scalar can potentially act as a dark matter (DM) candidate. Despite the remarkable success of the SM in explaining various phenomena observed in particle experiments and astrophysical studies, the mystery surrounding the nature of dark matter remains a significant unresolved issue [34–36]. Among the different candidates, the Weakly Interacting Massive Particle (WIMP) framework is notable for its ability to naturally account for the observed dark matter relic abundance, with $\Omega h^2 = 0.1198 \pm 0.0026$ [35], achieved through thermal freeze-out with an annihilation cross-section typical of the electroweak scale. This intriguing correlation hints at the possibility of new physics emerging at or above the weak scale. The validity of the WIMP paradigm has been extensively assessed using various methods, including direct detection [37–42], indirect detection [43–50], and collider searches [51–58]. Nevertheless, the absence of definitive signals has led to a growing interest in exploring alternative dark matter scenarios beyond the conventional WIMP framework.

An appealing alternative to the traditional WIMP scenario is the coannihilation mechanism [59, 60], which introduces an additional, heavier state named the coannihilation partner or dark matter partner that is closely related to the dark matter particle. In the specific case of inelastic dark matter (iDM) model, the coannihilation partner corresponds to an excited state, while the stable dark matter resides in the ground state [61–78]. These partners have the capability to interact with SM particles and, when combined with dark matter, can collectively undergo annihilation to produce SM particles. In this configuration, the strength of interaction between dark matter and SM particles can be significantly reduced or even nonexistent, leading to a diminished annihilation cross section for pairs of dark matter. This characteristic inherently aids in steering the model clear of stringent constraints imposed by observations from the Cosmic Microwave Background (CMB) [35, 79] and various indirect detection experiments [43, 45–48], which are sensitive to energy injection from late-time annihilations. Moreover, the feeble coupling to SM particles also enables the model to effectively bypass the limitations set by direct detection conducted in deep underground facilities [37–40].

In this research, we investigate a model of "purely" inelastic dark matter interaction involving the coannihilation mechanism. The dark sector comprises a complex scalar denoted as $\phi = \frac{1}{\sqrt{2}}(\phi_1 + i\phi_2)$, which interacts with SM particles through the Higgs boson. The "purely" means only the inelastic scattering interaction exists, or in other words, the tree-level elastic scattering interactions between the same dark sector scalars and the Higgs, ϕ_i–ϕ_i–Higgs, are absent. Previous studies on inelastic dark matter have mainly focused on light scalar or fermionic models with masses below 100 GeV. These works explored signals at present and future colliders, neutrino detectors, or astrophysical observations, and emphasized how the models account for the observed dark matter relic abundance [65, 67, 68, 70, 74, 76, 78, 80–83]. Other works studied heavier iDM models above 100 GeV, where annihilation between coannihilation partners dominates [84, 85]. These models can be probed at the upcoming High-Luminosity LHC (HL-LHC), and typically require moderate couplings between the dark sector and the Standard Model Higgs. Some studies also considered fermionic iDM models with additional scalar mediators, which can induce strongly first-order phase transitions and detectable collider signatures [86]. In contrast, our work, with a straightforward purely iDM model, not only addresses the dark matter relic abundance and (in-)direct detection signals, but also naturally includes possible first-order phase transitions and the consequent gravitational wave signals arising from the newly introduced scalar. Furthermore, if the mass splitting between the dark matter particle ϕ_1 and its excited partner ϕ_2 is small, the latter can behave as a long-lived particle (LLP) at collider scales [87]. In this case, hadron colliders can search for LLP signatures using displaced muon-jets or time-delayed techniques, which provide powerful tools for suppressing QCD backgrounds.

The structure of this paper is outlined as follows. In Sec. II, the scalar iDM model is discussed, and decay channels and lifetime of the DM partner are also calculated. In Sec. III, we investigate the DM relic abundance and various existing constraints from (in-)direct detection, thermalization requirement, collider searches, and Higgs precision measurements. In Sec. IV, we explore the electroweak phase transition with the new scalars and their possible gravitational waves. In Sec. V, the long-lived signatures of the DM partner ϕ_2 are studied. In Sec. VI, we conclude.

II. THE MODEL

In this work, we investigate a model of inelastic DM, which involves a complex scalar field, $\hat{\phi}$. This field is composed of two real scalar fields: $\hat{\phi}_1$ (the ground state) and $\hat{\phi}_2$ (the excited state). We place a hat on the field to distinguish it from its mass eigenstates. The excited state, $\hat{\phi}_2$, serves as a

DM partner of $\hat{\phi}_1$. The complex scalar field ϕ interacts with the SM Higgs field, H, via a quadratic coupling, and this coupling is in general complex. The interaction is described by the following Lagrangian:

$$\begin{aligned}\mathcal{L} = &\left(\partial_\mu \hat{\phi}\right)^\dagger \left(\partial^\mu \hat{\phi}\right) - \frac{1}{2}\mu_1^2 \hat{\phi}_1^2 - \frac{1}{2}\mu_2^2 \hat{\phi}_2^2 - \lambda_\phi \left(\hat{\phi}^\dagger \hat{\phi}\right)^2 - 2\lambda_I \hat{\phi}^2 |H|^2 + h.c. \\ &+ \mu^2 H^\dagger H - \lambda \left(H^\dagger H\right)^2 ,\end{aligned} \tag{1}$$

where $\lambda_I = \lambda_{I,r} + i\lambda_{I,i}$ is the complex coupling between the scalar field ϕ and the Higgs field, with $\lambda_{I,r}$ and $\lambda_{I,i}$ representing the real and imaginary components, respectively. Through this Higgs portal interaction, DM and its coannihilation partner interact with SM particles, mediated by the Higgs field. The Higgs field and the complex scalar $\hat{\phi}$ are expressed after electroweak symmetry breaking as:

$$H = \frac{1}{\sqrt{2}} \begin{pmatrix} H^+ \\ v_h + h + i\chi \end{pmatrix}, \quad \hat{\phi} = \frac{1}{\sqrt{2}} \left(\hat{\phi}_1 + i\hat{\phi}_2\right). \tag{2}$$

In this setup, only the Higgs field develops a vacuum expectation value (VEV), v_h, whereas the complex scalar $\hat{\phi}$ does not, protected by a discrete Z_2 symmetry under which only $\hat{\phi}$ is odd. The Goldstone bosons, $H^\pm$ and χ, are absorbed by the SM gauge bosons. After electroweak symmetry breaking, the mass matrix for $\hat{\phi}_1$ and $\hat{\phi}_2$ can be written as:

$$M = \begin{pmatrix} \mu_1^2 + 2\lambda_{I,r} v_h^2 & -2\lambda_{I,i} v_h^2 \\ -2\lambda_{I,i} v_h^2 & \mu_2^2 - 2\lambda_{I,r} v_h^2 \end{pmatrix}. \tag{3}$$

This mass matrix M can be diagonalized through a unitary rotation, U, such that:

$$U M U^\dagger = \mathrm{diag}(m_1^2, m_2^2), \tag{4}$$

where the rotation matrix U is given by:

$$U = \begin{pmatrix} \cos\theta & -\sin\theta \\ \sin\theta & \cos\theta \end{pmatrix}, \tag{5}$$

with the rotation angle satisfying

$$\tan(2\theta) = \frac{4\lambda_{I,i} v_h^2}{4\lambda_{I,r} v_h^2 + \mu_1^2 - \mu_2^2}. \tag{6}$$

With this rotation, we obtain the mass eigenstates ϕ_1 and ϕ_2 from the flavor eigenstates $\hat{\phi}_1$ and $\hat{\phi}_2$ as follows:

$$\begin{pmatrix}\phi_1\\ \phi_2\end{pmatrix} = U \cdot \begin{pmatrix}\hat{\phi}_1\\ \hat{\phi}_2\end{pmatrix}. \tag{7}$$

After rotating from the flavor eigenstates to the mass eigenstates, the couplings among mass eigenstates also need to be modified, which is relevant to the interaction term

$$\Delta\mathcal{L} = -\begin{pmatrix}\hat{\phi}_1 & \hat{\phi}_2\end{pmatrix}\begin{pmatrix}\lambda_{I,r} & -\lambda_{I,i}\\ -\lambda_{I,i} & -\lambda_{I,r}\end{pmatrix}\begin{pmatrix}\hat{\phi}_1\\ \hat{\phi}_2\end{pmatrix}\left(2v_h h + h^2\right) = \begin{pmatrix}\hat{\phi}_1 & \hat{\phi}_2\end{pmatrix}\hat{\Lambda}\begin{pmatrix}\hat{\phi}_1\\ \hat{\phi}_2\end{pmatrix}\left(2v_h h + h^2\right) \tag{8}$$

$$= (\phi_1 \;\; \phi_2)\, U\hat{\Lambda}U^\dagger \begin{pmatrix}\phi_1\\ \phi_2\end{pmatrix}\left(2v_h h + h^2\right) \tag{9}$$

where

$$\Lambda = U\hat{\Lambda}U^\dagger = \begin{pmatrix}\lambda_{11} & \lambda_{12}\\ \lambda_{21} & \lambda_{22}\end{pmatrix} = \cos(2\theta)\cdot\begin{pmatrix}\lambda_{I,i}\tan(2\theta) + \lambda_{I,r} & \tan(2\theta)\lambda_{I,r} - \lambda_{I,i}\\ \tan(2\theta)\lambda_{I,r} - \lambda_{I,i} & -\lambda_{I,i}\tan(2\theta) - \lambda_{I,r}\end{pmatrix} \tag{10}$$

It is clear that the coupling matrix, Λ and $\hat{\Lambda}$, are both traceless, which implies that the interactions between $\hat{\phi}_1\hat{\phi}_1 h$ and $\hat{\phi}_2\hat{\phi}_2 h$ have opposite signs, both before and after diagonalization.

Direct detection (DD) experiments impose stringent constraints on the scattering cross-section between DM and SM particles. To evade these constraints, it is crucial that the direct quartic interaction between DM and SM particles is minimized. This can be achieved by setting the direct interaction term $\lambda_{11} = 0$ from the Lagrangian. Thus, we require that the transformation angle θ satisfy the condition:

$$\tan(2\theta) = -\frac{\lambda_{I,r}}{\lambda_{I,i}}. \tag{11}$$

Substituting this into Eq. (6), we obtain the following relation:

$$-\frac{\lambda_{I,r}}{\lambda_{I,i}} = \frac{4\lambda_{I,i}v_h^2}{4\lambda_{I,r}v_h^2 + \mu_1^2 - \mu_2^2}, \tag{12}$$

which leads to

$$\lambda_{I,i} = \pm\frac{1}{2v_h}\sqrt{(\mu_2^2 - \mu_1^2 - 4\lambda_{I,r}v_h^2)\lambda_{I,r}}. \tag{13}$$

With this relationship, the coupling matrix will be simplified to:

$$\Lambda = \begin{pmatrix} 0 & \mp\frac{1}{2v_h}\sqrt{\left(\mu_2^2-\mu_1^2\right)\lambda_{I,r}} \\ \mp\frac{1}{2v_h}\sqrt{\left(\mu_2^2-\mu_1^2\right)\lambda_{I,r}} & 0 \end{pmatrix}, \tag{14}$$

and the physical masses of ϕ_1 and ϕ_2 are

$$m_1^2 = \frac{1}{2}\Big(\mu_1^2+\mu_2^2- \sqrt{(\mu_1^2-\mu_2^2+4\,\lambda_{\rm I,r}\,v_h^2)\left(\mu_1^2-\mu_2^2\right)}\ \Big), \tag{15}$$

$$m_2^2 = \frac{1}{2}\Big(\mu_1^2+\mu_2^2+ \sqrt{(\mu_1^2-\mu_2^2+4\,\lambda_{\rm I,r}\,v_h^2)\left(\mu_1^2-\mu_2^2\right)}\ \Big). \tag{16}$$

By nullifying the direct interaction coupling λ_{11}, we get a purely iDM model. In the mass eigenstate basis, the effective Lagrangian can be written as:

$$\mathcal{L} = \frac{1}{2}\partial_\mu\phi_1\partial^\mu\phi_1 + \frac{1}{2}\partial_\mu\phi_2\partial^\mu\phi_2 - \frac{1}{2}m_1^2\phi_1^2 - \frac{1}{2}m_2^2\phi_2^2 - \lambda_{12}\phi_1\phi_2(2v_h h + h^2) - \lambda_\phi(\phi^\dagger\phi)^2 - V(h), \tag{17}$$

where

$$\lambda_{12} = \mp\frac{\sqrt{(\mu_2^2-\mu_1^2)\lambda_{I,r}}}{v_h}. \tag{18}$$

We can introduce a dimensionless parameter to represent the mass splitting between the two real scalar fields:

$$\Delta \equiv \frac{m_2-m_1}{m_1}, \tag{19}$$

Thus, there are 4 free physical parameters of Lagrangian (17):

$$\{m_1, \Delta, \lambda_{12}, \lambda_\phi\}. \tag{20}$$

In the rest of the paper, we occasionally retain the notation m_2 to simplify the mathematical expressions. Finally, we can express the initial parameters in terms of the physical ones using the following relations:

$$\lambda_{I,r} = \frac{v_h^2\lambda_{12}^2}{\sqrt{(m_2^2-m_1^2)^2+4v_h^4\lambda_{12}^2}}, \tag{21}$$

$$\lambda_{I,i} = \pm\frac{1}{2v_h}\sqrt{(\mu_2^2-\mu_1^2-4\lambda_{I,r}v_h^2)\lambda_{I,r}}, \tag{22}$$

$$\mu_2^2 = \frac{1}{2}\left((m_1^2 + m_2^2) + \sqrt{(m_2^2 - m_1^2)^2 + 4v_h^4\lambda_{12}^2}\right), \tag{23}$$

$$\mu_1^2 = \frac{1}{2}\left((m_1^2 + m_2^2) - \sqrt{(m_2^2 - m_1^2)^2 + 4v_h^4\lambda_{12}^2}\right). \tag{24}$$

A. Decay Processes and Branching Ratios of Inelastic Dark Matter Partners

Due to the interaction between ϕ_1, ϕ_2 and Higgs, ϕ_2 can decay into $\phi_1 h$ if kinematically allowed. In our study, we are interested in $\Delta \times m_1 < m_h$, so that ϕ_2 can only decay into an off-shell Higgs, which then undergoes a two-body decay into SM particles.

The decay width of ϕ_2 is influenced by several factors, including the small mass difference Δ, the weak Yukawa coupling between SM fermions and the Higgs boson, and the presence of an off-shell Higgs mass. These factors may result in ϕ_2 being long-lived under certain conditions. In the following analysis, we will systematically calculate the decay width of ϕ_2 for each decay channel. The decay process can generally be categorized into two main channels: the leptonic and the hadronic channels.

Before delving into the calculations, it is crucial to consider the scenario where the mass difference is significantly larger than the relevant energy scale (2 GeV) of the perturbative spectator model [88, 89] and the fermion mass, $\Delta \cdot m_1 \gg 2$ GeV and $\Delta \cdot m_1 \gg 2m_f$, where the partial decay width of $\phi_2 \to \phi_1 f\bar{f}$ can be reasonably approximated as follows:

$$\Gamma(\phi_2 \to \phi_1 f\bar{f}) \simeq \frac{\lambda_{12}^2 m_f^2 m_2^3 \Delta^5}{60\pi^3 m_h^4} \times \theta(m_1 \cdot \Delta - 2m_f), \tag{25}$$

where the fermion mass m_f is neglected for phase space integration. This approximation remains valid for the leptonic decay channels as long as $m_1 \cdot \Delta \gg 2m_f$, even when $m_1 \cdot \Delta < 2$ GeV.

However, when the fermion mass m_f is comparable to the mass splitting $m_1 \cdot \Delta$, numerical integration over the phase space is necessary. For the kinematically allowed leptonic decay channel, the complete decay width can be determined as:

$$\Gamma(\phi_2 \to \phi_1 \ell^+\ell^-) = \frac{8m_\ell^2\lambda_{12}^2}{(2\pi)^3 32 m_2^3} \int_{4m_\ell^2}^{m_1^2\Delta^2} \frac{(s_{12} - 4m_\ell^2)^{3/2}\sqrt{\frac{m_1^4 + (m_2^2 - s_{12})^2 - 2m_1^2(m_2^2 + s_{12})}{s_{12}}}}{(s_{12} - m_h^2)^2} ds_{12}, \tag{26}$$

where s_{12} represents the invariant mass of the final lepton pair. Specifically, we focus on the muon final state due to its considerable branching ratio and distinct signals observable at the HL-LHC.

And the SM backgrounds can be effectively reduced through targeted selection criteria.

For mass differences smaller than 2 GeV, the calculation becomes somewhat intricate and requires careful consideration, especially concerning the types of fermions present. In the case of hadronic decay channels, only the total hadronic decay width is of significance, as it allows for the determination of the overall decay width. These calculations often require accounting for non-perturbative effects.

Considering Ref. [89], the integral range of s_{12} can be split into two segments: one from $(2m_{\text{final}})^2$ to $(2\text{ GeV})^2$, where m_{final} is the mass of the SM particle from ϕ_2 decays and $2m_{\text{final}} < 2$ GeV, and the other extending beyond $(2\text{ GeV})^2$. In the former range, the methodology of chiral perturbation theory elucidated in Ref. [89] is utilized to compute the amplitudes for diverse decay processes, such as $\phi_2 \to \phi_1\pi\pi$, $\phi_2 \to \phi_1 KK$, $\phi_2 \to \phi_1\eta\eta$ $(\rho\rho)$, among others. In the latter range, the parton-level amplitude is good enough, which can be directly derived following the Feynman rules of QCD. In accordance with Ref. [89], all feasible channels, like $\phi_2 \to \phi_1 gg$, $\phi_2 \to \phi_1 c\bar{c}$, $\phi_2 \to \phi_1 s\bar{s}$, $\phi_2 \to \phi_1 b\bar{b}$, are computed. By summing the contributions from all relevant decay channels in each interval and integrating over s_{12} for each segment separately, the total width of the hadronic channel can be determined.

One might wonder whether the photon channel should be included in the calculation of the total decay width, similar to the significance of the SM Higgs discovery at the LHC [1], where the branching ratio $Br(h \to \gamma\gamma)$ is around 0.2%. In our model, it is observed that the branching ratio of $\phi_2 \to \phi_1\gamma\gamma$ falls within the range of $[2.5\times 10^{-5}, 2.6\times 10^{-4}]$ for $m_2 \in [50, 120]$ with $\Delta = 0.05$, significantly smaller than the decay width of channel $\phi_2 \to \phi_1 gg$ by about three orders of magnitude. While the photon channel benefits from a clean SM background, it suffers from a much lower branching ratio and greater challenges in track reconstruction compared to the muon channel. For this reason, our collider study will focus on the muon channel, and the determination of the total decay width and branching ratio for the muon pair will take priority.

In Fig. 1, we show the proper decay length (left panel), $c\tau_{\phi_2} = 1/\Gamma_{tot}$, and the branching ratio $Br(\phi_2 \to \phi_1\mu^+\mu^-)$ (right panel) for three different mass splittings. For the mass range of interest, $m_2 \in [50, 110]$ GeV, the rescaled proper decay length for $\Delta = 0.05$ spans from 10^{-2} cm to 7 cm. This suggests that the dark matter partner ϕ_2 could be long-lived at collider scales, provided that λ_{12} is on the order of 0.1. However, for larger values of Δ, the decay length decreases by several orders of magnitude, making it challenging to observe a displaced or delayed signal unless λ_{12} is extremely small. Regarding the branching ratio $Br(\phi_2 \to \phi_1\mu^+\mu^-)$, it stretches from 1% to 30%

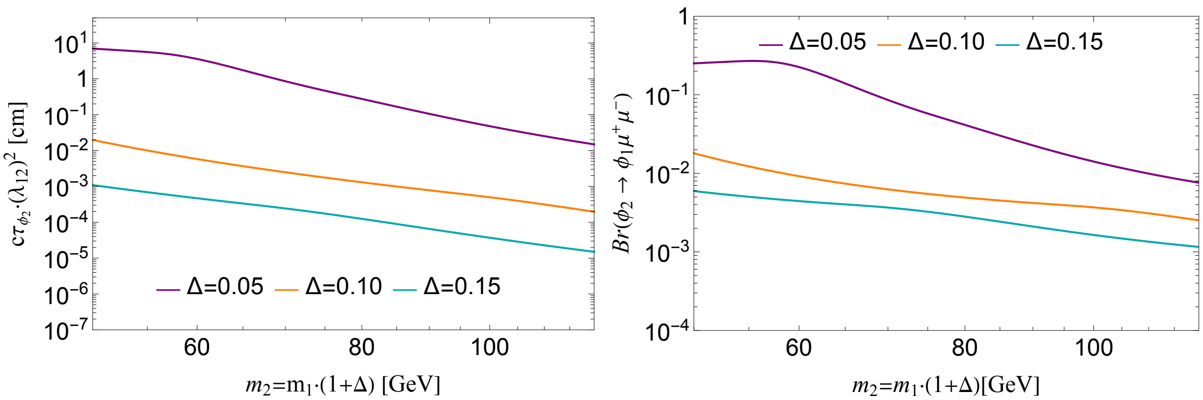

FIG. 1. Total decay width and branching ratio of muon pair final state of DM partner as a function of its mass for three different mass splittings. The purple line represents the results of mass splitting $\Delta = 0.05$, the orange one represents the results of $\Delta = 0.10$, and the cyan one corresponds to $\Delta = 0.15$.

for the cases shown. In contrast, for the other two scenarios, the branching ratios are significantly smaller, making detection more difficult at colliders. Another concern is whether prompt decays of the DM partners could be observed, especially in scenarios with large mass differences. In particular, prompt decays leading to muon pairs could produce signals like monojet plus a muon pair, accompanied by substantial missing transverse energy, $j + \not{E}_T + \mu^+\mu^-$, is feasible. However, these prompt decay signatures are often overwhelmed by large Standard Model backgrounds, complicating detection at proton-proton colliders. Therefore, we focus initially on the long-lived signatures of the DM partner, with the exploration of prompt decay signatures left for future research.

It is important to note that the branching ratios of alternative decay channels, such as $\phi_2 \to \phi_1\tau^+\tau^-$, $\phi_2 \to \phi_1\pi\pi$, and other jet channels, can also be computed. Particularly significant are the $\phi_2 \to \phi_1 c\bar{c}$ and $\phi_2 \to \phi_1\tau^+\tau^-$channels, which become dominant for $m_2 \gtrsim 60$GeV and 80 GeV , respectively. However, due to the small mass differences involved, the jets produced in these decays are too soft to be detected, and therefore, these channels are not considered further here. In contrast, the muon final state benefits from a lower p_T trigger, which facilitates easier reconstruction and better separation from QCD backgrounds. This makes the muon channel a highly effective search channel at pp colliders. A more detailed exploration of collider searches will be provided in the following section.

III. DARK MATTER AND EXISTING CONSTRAINTS

A. Dark Matter Relic Abundance

In our model, both ϕ_1 and ϕ_2 can contribute to the DM relic abundance via the coannihilation process [90]. Assuming that the number density ratio between ϕ_1 and ϕ_2 follows its equilibrium value, the system reduces to an effective single-species Boltzmann equation, which can be solved using the effective annihilation cross section,

$$\sigma_{\rm eff} = \frac{g_{\phi_1}^2}{g_{\rm eff}^2}\left(\sigma_{11} + 2\sigma_{12}\frac{g_{\phi_2}}{g_{\phi_1}}\,(1+\Delta)^{3/2}\,e^{-x\cdot\Delta} + \sigma_{22}\frac{g_{\phi_2}^2}{g_{\phi_1}^2}\,(1+\Delta)^3\,e^{-2x\cdot\Delta}\right), \tag{27}$$

where $\sigma = \sigma(\phi_i\phi_j \to \text{SM SM})$ denotes the annihilation cross section into SM particles, $g_{\phi_1} = g_{\phi_2}$ represent the intrinsic degrees of freedom of ϕ_1 and ϕ_2, $x = m_1/T$ with T being the temperature of the thermal bath. The effective degree of freedom $g_{\rm eff}$ is defined as

$$g_{\rm eff} = g_{\phi_1} + g_{\phi_2}\,(1+\Delta)^{3/2}\,e^{-x\cdot\Delta}. \tag{28}$$

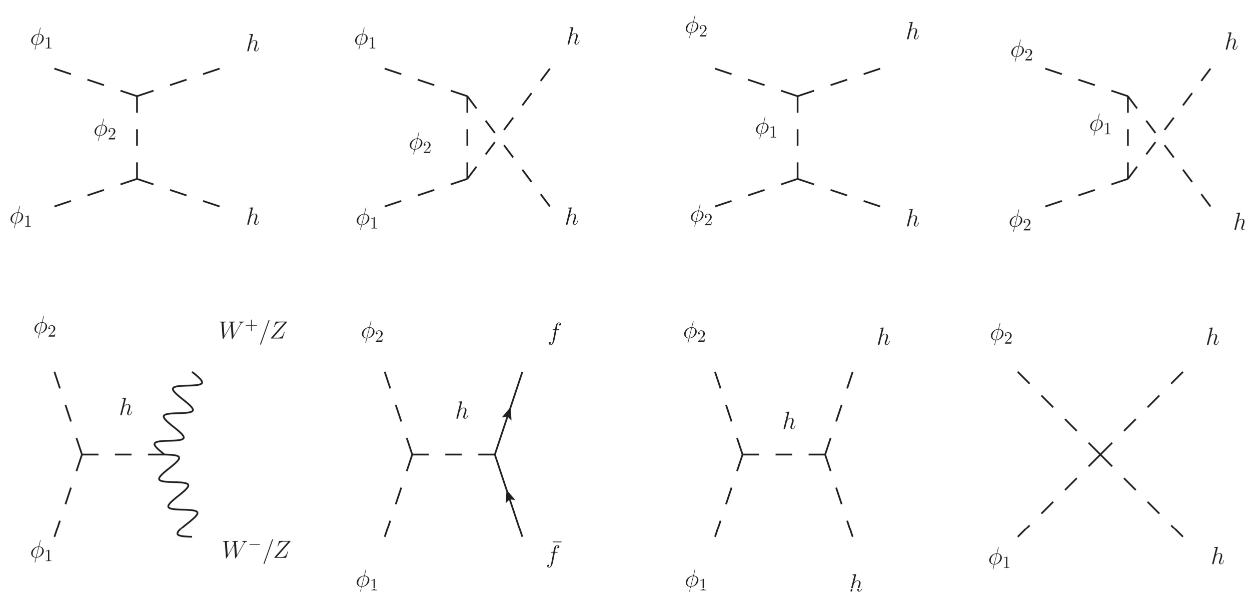

FIG. 2. Feynman diagrams for the annihilation processes $\phi_i\phi_j \to$ SM SM

The annihilation processes $\phi_i\phi_j \to$ SM SM include final states such as $\bar{f}f$, W^+W^-, ZZ, and hh.

Their corresponding Feynman diagrams are shown in Fig. 2. The total s-wave contributions to the annihilation cross sections, denoted by $\langle \sigma v \rangle_s$, can be computed as follows:

$$\langle \sigma v \rangle_s = \langle \sigma v \rangle_{f\bar{f}} + \langle \sigma v \rangle_{WW} + \langle \sigma v \rangle_{ZZ} + \langle \sigma v \rangle_{hh}, \tag{29}$$

which includes four processes are proportional to λ_{12}^2

$$\begin{aligned}
\langle \sigma v \rangle_{f\bar{f}} &\simeq \frac{\lambda_{12}^2\, m_f^2 \left((m_1+m_2)^2 - 4\, m_f^2\right)^{3/2}}{2\pi \sqrt{m_1\, m_2}\,(m_1+m_2)^2\,(m_1+m_2-m_h)^2\,(m_1+m_2+m_h)^2},\\
\langle \sigma v \rangle_{WW} &\simeq \frac{\lambda_{12}^2 \sqrt{(m_1+m_2)^2 - 4m_W^2}\left(-4m_W^2(m_1+m_2)^2 + (m_1+m_2)^4 + 12m_W^4\right)}{4\pi \sqrt{m_1 m_2}(m_1+m_2)^2(m_1+m_2-m_h)^2(m_1+m_2+m_h)^2},\\
\langle \sigma v \rangle_{ZZ} &\simeq \frac{\lambda_{12}^2 \sqrt{(m_1+m_2)^2 - 4m_Z^2}\left(-4m_Z^2(m_1+m_2)^2 + (m_1+m_2)^4 + 12m_Z^4\right)}{4\pi \sqrt{m_1 m_2}(m_1+m_2)^2(m_1+m_2-m_h)^2(m_1+m_2+m_h)^2},\\
\langle \sigma v \rangle_{\phi_1\phi_2\to hh} &\simeq \frac{\lambda_{12}^2 \sqrt{(m_1+m_2)^2 - 4m_h^2}\left((m_1+m_2)^2 + 2m_h^2\right)^2}{4\pi \sqrt{m_1 m_2}(m_1+m_2)^2(m_1+m_2-m_h)^2(m_1+m_2+m_h)^2},
\end{aligned} \tag{30}$$

and two processes are proportional to λ_{12}^4:

$$\begin{aligned}
\langle \sigma v \rangle_{\phi_1\phi_1\to hh} &\simeq \frac{\lambda_{12}^4 v_h^4 \sqrt{m_1^2 - m_h^2}}{\pi m_1^3 \left(m_h^2 - (m_1^2 + m_2^2)\right)^2},\\
\langle \sigma v \rangle_{\phi_2\phi_2\to hh} &\simeq \frac{\lambda_{12}^4 v_h^4 \sqrt{m_2^2 - m_h^2}}{\pi (\Delta+1)^3 m_1^3 \left(m_h^2 - (m_1^2 + m_2^2)\right)^2}.
\end{aligned} \tag{31}$$

The freeze-out temperature is determined by

$$x_f = \ln \frac{0.038\; g_{\rm eff}\; m_{\rm Pl}\; m_1 \langle \sigma_{\rm eff} v \rangle}{g_*^{1/2} x_f^{1/2}}. \tag{32}$$

While the relic abundance is given by

$$\Omega h^2 = \frac{1.07 \times 10^9}{g_*^{1/2} J(x_f) m_{\rm Pl}({\rm GeV})}, \tag{33}$$

where g_* is the total degree of freedom of the thermal universe, $m_{\rm Pl}$ is the Planck mass, and the function $J(x_f)$ is defined as

$$J(x_f) = \int_{x_f}^{\infty} \frac{\langle \sigma_{\text{eff}} v \rangle}{x^2}\, dx. \tag{34}$$

We fix the relic density to the observed value $\Omega h^2 = 0.1198$ [91] by iteratively determining the freeze-out temperature x_f and the coupling constant λ_{12} for various total mass choices $m_{tot} = m_1 + m_2$. The resulting parameter-space curves in the (λ_{12}, m_{tot}) plane for $\Delta = 0.05$ (purple line) and 0.15 (cyan line) are illustrated in the right panel of Fig. 3 for $m_{tot} \in [60, 220]$ GeV. A pronounced dip occurs at $m_{tot} \simeq m_h$ due to the Higgs resonance, while additional sharp features at $m_{tot} \simeq 160$ GeV and $m_{tot} \simeq 180$ GeV correspond to the opening of the W^+W^- and ZZ production channels, respectively.

B. Existing Constraints

Apart from the requirement of the DM relic abundance, the interaction between the Higgs boson and the new iDM scalars induces many direct, indirect and collider search constraints. In this section, we will mainly discuss the limits on the iDM model from DM (in-)direct detection, thermalization of its excited state, monojet+$\not{E}_T$ searches, and Higgs precision measurements.

1. *DM (in-)direct detection*

In our scenario, the DM ϕ_1 couples to SM only via the $\phi_1\phi_2 H$ interaction, does not directly couple with the SM fermions or gluons, so the tree-level DM-nucleus/electron elastic scattering processes are forbidden. As to the excited state ϕ_2, after decoupling with the thermal bath in the early universe, it completely decayed into DM and SM particles, leaving no remnants in today's universe. Consequently, no significant signals from ϕ_2 are expected in direct detection experiments. However, the one-loop diagram of two λ_{12} vertices can induce an effective $\phi_1\phi_1 h^2$ interaction [92], whose interaction strength is smaller than $\sim (\lambda_{12}/4\pi)^2$. For our interested parameter region, $\lambda_{12} < 0.6$, the effective interaction strength should be smaller than 2.3×10^{-3}, which is too small to provide any meaningful constraints for direct detection. Another possibility to consider is whether the upscattering process $\phi_1 N \to \phi_2 N$ could contribute to direct detection signals. However, the typical mass splitting $\Delta m = m_1 \cdot \Delta \gtrsim 1$GeV is much larger than the kinetic energy of the non-relativistic ϕ_1, making up-scattering kinematically forbidden. Overall, this iDM model is free from direct detection constraints.

While for the indirect detection, as demonstrated previously, the ϕ_2 totally decayed before BBN, thus they do not inject energy into the thermal bath during the BBN era. Therefore, they do not change the evolution of the universe. While for $m_1 > m_h$, DM ϕ_1 can annihilate to a pair of Higgs bosons via t-channel ϕ_2, which in principle can place a limit on λ_{12}. However, this process is suppressed by a factor $\lambda_{12}^4 \sim 10^{-4}$ [93], thus the cross-section is very small. For $m_1 < m_h$, this process is directly kinematically forbidden. Therefore, due to the non-existent ϕ_2 in the late universe, the tiny annihilation cross section of $\phi_1\phi_1 \to hh$ and the kinematical requirement, the indirect detection cannot impose any restrictions on our interested parameter spaces.

2. *Monojet+$\not{E}_T$ searches*

In our model, both ϕ_1 and ϕ_2 couple to the SM via interactions with the Higgs boson, implying potential constraints from collider searches. In particular, the process $pp \to h^* j \to \phi_1\phi_2 j$, followed by $\phi_2 \to \phi_1 jj$, can be produced at the LHC. However, because the mass difference $\Delta \cdot m_1$ is small, the jets from ϕ_2 decay are soft and cannot be efficiently reconstructed. Consequently, the final state consists of DM and low-energy jets that escape detection, contributing to a missing transverse energy ($\not{E}_T$). Only the initial jet along with the Higgs production is sufficiently energetic to be observed, leading to a mono-jet signature characterized by a high-p_T jet and large $\not{E}_T$ ($j + \not{E}_T$), distinguishing it from the SM background.

The ATLAS and CMS collaborations have performed extensive searches for DM in the mono-jet plus missing energy channel [94–98]. The ATLAS analysis in Ref. [96], based on 139 fb^{-1} of data at $\sqrt{s} = 13$ TeV, requires at least one jet with $p_T(j_1) > 200$ GeV and $\not{E}_T > 200$ GeV. At 95% confidence level (C.L.), the model-independent upper limit on the cross-section for non-SM production is ~ 0.7 pb. While for the CMS [97, 98], it gives a much weaker constraint than ATLAS due to its smaller data luminosity. Therefore, we will mainly focus on ATLAS.

By comparing this bound with theoretical predictions obtained using `MadGraph5_aMC@NLO` [99, 100], we can constrain the coupling λ_{12} for given m_1 and m_2. In our scenario, for $m_1+m_2 > m_h$, the corresponding upper limit on λ_{12} is larger than the value required to reproduce the observed relic abundance. For example, with $\Delta = 0.1$ and $m_1 = 80$ GeV, the predicted cross-section times efficiency computed with `MadGraph` for the relic abundance motivated coupling is 7.6×10^{-5} pb, which is far below the current experimental sensitivity of 0.7 pb. Therefore, our model naturally evades existing mono-jet plus missing energy constraints.

3. *Higgs precision measurements*

Because the scalar fields ϕ_1 and ϕ_2 interact with the SM Higgs boson, constraints from Higgs precision measurements must be taken into account. A particularly relevant bound arises from the Higgs total decay width: the combined branching ratio into nonstandard final states is constrained to be below 8.4% at the 95% C.L. [101, 102]. If the mass condition $m_1 + m_2 < m_h$ is satisfied, the SM Higgs can decay directly into ϕ_1 and ϕ_2, with the corresponding partial width given by

$$\Gamma(h \to \phi_1\phi_2) = \frac{\lambda_{12}^2 v_h^2 \sqrt{\left((m_h - m_2)^2 - m_1^2\right)\left((m_h + m_2)^2 - m_1^2\right)}}{16\pi m_h^3}. \tag{35}$$

And its branching ratio can be written as

$$\mathrm{Br}(h \to \phi_1\phi_2) = \frac{\Gamma(h \to \phi_1\phi_2)}{\Gamma(h \to \mathrm{SM\ SM}) + \Gamma(h \to \phi_1\phi_2)}, \tag{36}$$

where $\Gamma(h \to \mathrm{SM\ SM})$ is the Higgs total decay width in SM. By requiring that $\mathrm{Br}(h \to \phi_1\phi_2) <$ 8.4%, the constraint can be obtained, which excludes most of the parameter space where $\lambda_{12} > 5.5 \times 10^{-3}$ and $m_1 + m_2 < m_h$. If $2m_1 < m_h < m_1 + m_2$, the Higgs can decay via an off-shell ϕ_2: $h \to \phi_1\phi_2^* \to \phi_1\phi_1 + \mathrm{SM\ SM}$, which is suppressed by the tiny mass splitting and the multi-body phase space. Numerical calculation shows the decay width for $\Delta = 0.1$ is smaller than 10^{-7} MeV when $\lambda_{12} = 1$, indicating that it cannot impose any meaningful constraint on the parameter space consistent with the DM relic abundance. If $m_h < 2m_1$, then even the off-shell decay to $\phi_1\phi_1 + \mathrm{SM\ SM}$ is kinematically forbidden. Therefore, in summary, for total mass ($m_{tot} = m_1 + m_2$) above the Higgs mass, Higgs precision measurements can not provide any effective constraints on the parameter regions corresponding to the correct dark matter relic density.

In addition, the Higgs invisible decay provides a stringent constraint on the coupling λ_{12} when $m_1 + m_2 < m_h$. This is because, in this case, the decay products ϕ_1 and ϕ_2 typically lead to soft jets or undetectable final states, making them appear as missing energy. The branching ratio for this invisible-like channel has the same form as Eq. (36). Combined with Eq. (35), this invisible decay constraint can be derived. The projected upper limit on Higgs invisible decay at future

CEPC is 0.24% at the 95% confidence level [103]. Conservatively, we require $Br(h \to \phi_1\phi_2) < Br(h \to \text{Inv}) < 0.24\%$ for the region $m_1 + m_2 < m_h$, which typically requires $\lambda_{12} \lesssim 9 \times 10^{-4}$. These constraints are illustrated in the shaded regions of the right panel in Fig. 4. In the region where $m_h < 2m_1$, the decay is kinematically forbidden, and therefore, no constraints are applicable in this area. For the mass region, $2m_1 < m_h < m_1 + m_2$, although the four-body decay process, $h \to \phi_1\phi_2^* \to \phi_1\phi_1$SM SM, is possible, its decay width is too small to impose any constraints due to the heavy suppression from multi-particle final state phase space and heavy mediator mass.

IV. ELECTROWEAK PHASE TRANSITION AND GRAVITATIONAL WAVES

In this section, we will examine the vacuum structure and the thermal evolution of the model. We begin by analyzing the total scalar potential at zero temperature. The potential incorporates contributions from the SM Higgs doublet and the two real scalar fields $\hat{\phi}_1$ and $\hat{\phi}_2$. The general form of the potential, as given in Eq. (1), is

$$\begin{aligned} V(\hat{\phi}_1, \hat{\phi}_2, H) =& \frac{1}{2}\mu_1^2\hat{\phi}_1^2 + \frac{1}{2}\mu_2^2\hat{\phi}_2^2 + \frac{\lambda_\phi}{4}(\hat{\phi}_1^2 + \hat{\phi}_2^2)^2 + \lambda_I(\hat{\phi}_1^2 - \hat{\phi}_2^2 + 2i\hat{\phi}_1\hat{\phi}_2)|H|^2 + h.c. \\ & - \mu^2|H|^2 + \lambda|H|^4. \end{aligned} \tag{37}$$

As outlined in Eq. (20), the model contains four free parameters $\{m_1, \Delta, \lambda_\phi, \lambda_{12}\}$. However, since λ_{12} is determined by the DM relic abundance, only three parameters remain independent: $\{m_1, \Delta, \lambda_\phi\}$. The relations between these parameters, prior to field rotation, are given in Eq.(24).

We impose the vacuum conditions at zero temperature:

$$\langle\hat{\phi}_1\rangle = \langle\hat{\phi}_2\rangle = 0, \quad \langle h\rangle = v_h, \tag{38}$$

ensuring the model reproduces the observed electroweak vacuum. This constraint further restricts the allowed parameter space.

From the physical Lagrangian in Eq. (17), we can see a negative coupling coefficient $\lambda_{12} < 0$ can destabilize the SM vacuum at $(h, \hat{\phi}_1, \hat{\phi}_2) = (v_h, 0, 0)$, making it potentially metastable or even unstable. To ensure that electroweak symmetry breaking corresponds to the true vacuum of the theory, we begin our analysis from the physical scalar potential:

$$V(h, \phi_1, \phi_2) = \frac{1}{2}m_1^2\phi_1^2 + \frac{1}{2}m_2^2\phi_2^2 + \lambda_{12}\phi_1\phi_2(2v_h h + h^2) + \lambda_\phi(\phi^\dagger\phi)^2 + V(h). \tag{39}$$

To explore the symmetry properties of the quartic interactions and their implications for vacuum stability, we consider the case where the scalar fields are aligned, $\phi_2 = \pm\phi_1$. In this limit, the quartic part of the potential simplifies to:

$$\pm\lambda_{12}\phi_1^2 h^2 + \lambda_\phi\phi_1^4 + \frac{\lambda}{4}h^4 = \begin{pmatrix} h^2 & \phi_1^2 \end{pmatrix} \begin{pmatrix} \frac{\lambda}{4} & \pm\frac{1}{2}\lambda_{12} \\ \pm\frac{1}{2}\lambda_{12} & \lambda_\phi \end{pmatrix} \begin{pmatrix} h^2 \\ \phi_1^2 \end{pmatrix}. \tag{40}$$

To make sure the SM vacuum is the true vacuum, we need the determinant of the above coefficient matrix to be positive, which leads to the constraint

$$|\lambda_{12}| < \sqrt{\lambda_\phi \lambda}, \tag{41}$$

which ensures that the scalar potential remains stable and that the SM vacuum remains the true vacuum of the theory.

In the early high-temperature universe, the scalar potential receives thermal corrections due to interactions with the hot plasma. Using the high-temperature expansion and retaining terms up to order T^4, the gauge-invariant finite-temperature effective potential can be written as [104]

$$V_T(\phi_1, \phi_2, h, T) = V_T^{\text{Higgs}} + V_T^{\text{BSM}}, \tag{42}$$

where Higgs potential V_T^{Higgs} is determined by

$$\begin{aligned} V_T^{\text{Higgs}} =& D(T^2 - T_0^2)h^2 - ETh^3 + \frac{\lambda(T)}{4}h^4 + \frac{3m_h^2 h^2}{16v_h^2}\left(\frac{T^2}{3} + \frac{m_h^2}{4\pi^2} + \frac{m_h^2 T^2}{32\pi^2 v_h^2}\right) \\ &+ \left(\frac{T^2}{24} + \frac{m_h^2}{32\pi^2} + \frac{m_h^2 T^2}{256\pi^2 v_h^2}\right)\left(\lambda_{I,r}(\phi_1^2 - \phi_2^2) - 2\lambda_{I,i}\phi_1\phi_2\right) \\ &- \frac{T}{12\pi}\left(-\frac{m_h^2}{2} + 3\lambda h^2 + \lambda_{I,r}(\phi_1^2 - \phi_2^2) - 2\lambda_{I,i}\phi_1\phi_2 + \frac{\lambda}{4}T^2\right)^{3/2} \\ &- \frac{1}{64\pi^2}\left(-\frac{m_h^2}{2} + 3\lambda h^2 + \lambda_{I,r}(\phi_1^2 - \phi_2^2) - 2\lambda_{I,i}\phi_1\phi_2 + \frac{\lambda}{4}T^2\right)^2 \ln\frac{m_h^2 + \frac{\lambda}{4}T^2}{A_B T^2}, \end{aligned} \tag{43}$$

and BSM potential V_T^{BSM} is defined as

$$
\begin{aligned}
V_T^{\rm BSM} =& \frac{T^2}{24}\left(4\lambda_\phi\phi_1^2+4\lambda_\phi\phi_2^2\right)-\frac{T}{12\pi}(\mu_1^2+3\lambda_\phi\phi_1^2+\lambda_\phi\phi_2^2+2\lambda_{I,r}h^2+\frac{T^2}{3}\lambda_\phi)^{3/2}\\
&+\frac{1}{32\pi^2}(\mu_1^2+3\lambda_\phi\phi_1^2+\lambda_\phi\phi_2^2+2\lambda_{I,r}h^2+\frac{T^2}{3}\lambda_\phi)(\mu_1^2+2\lambda_{I,r}v_h^2+\frac{T^2}{3}\lambda_\phi)\\
&-\frac{T}{12\pi}(\mu_2^2+3\lambda_\phi\phi_2^2+\lambda_\phi\phi_1^2-2\lambda_{I,r}h^2+\frac{T^2}{3}\lambda_\phi)^{3/2}\\
&+\frac{1}{32\pi^2}(\mu_2^2+3\lambda_\phi\phi_2^2+\lambda_\phi\phi_1^2-2\lambda_{I,r}h^2+\frac{T^2}{3}\lambda_\phi)(\mu_2^2-2\lambda_{I,r}v_h^2+\frac{T^2}{3}\lambda_\phi)\\
&-\frac{1}{64\pi^2}(\mu_1^2+3\lambda_\phi\phi_1^2+\lambda_\phi\phi_2^2+2\lambda_{I,r}h^2+\frac{T^2}{3}\lambda_\phi)^2\ln\frac{\mu_1^2+2\lambda_{I,r}v_h^2+\frac{T^2}{3}\lambda_\phi}{A_BT^2}\\
&-\frac{1}{64\pi^2}(\mu_2^2+3\lambda_\phi\phi_2^2+\lambda_\phi\phi_1^2-2\lambda_{I,r}h^2+\frac{T^2}{3}\lambda_\phi)^2\ln\frac{\mu_2^2-2\lambda_{I,r}v_h^2+\frac{T^2}{3}\lambda_\phi}{A_BT^2}\\
&+\frac{1}{2}\mu_1^2\phi_1^2+\frac{1}{2}\mu_2^2\phi_2^2+\frac{\lambda_\phi}{4}(\phi_1^2+\phi_2^2)^2+\lambda_{I,r}(\phi_1^2-\phi_2^2)h^2-2\lambda_{I,i}\phi_1\phi_2h^2, \qquad (44)
\end{aligned}
$$

where the key parameters are given by

$$
\begin{aligned}
D &= \frac{2m_W^2+m_Z^2+2m_t^2}{8v_h^2},\ E=\frac{2m_W^3+m_Z^3}{4\pi v_h^3},\\
T_0^2 &= \frac{m_h^2-8Bv_h^2}{4D},\ B=\frac{3}{64\pi^2v_h^4}(2m_W^4+m_Z^4-4m_t^4),\\
\lambda(T) &= \lambda-\frac{3}{16\pi^2v_h^4}(2m_W^4\ln\frac{m_W^2}{A_BT^2}+m_Z^4\ln\frac{m_Z^2}{A_BT^2}-4m_t^4\ln\frac{m_t^2}{A_FT^2}),\\
\ln A_B &= \ln a_b-3/2,\ \ \ln A_F=\ln a_f-3/2, \lambda=\frac{m_h^2}{2v^2}.
\end{aligned} \qquad (45)
$$

The constants $a_b = 16\pi^2 e^{3/2-2\gamma_E}$ and $a_f = \pi^2 e^{3/2-2\gamma_E}$ correspond to the gauge and fermion contributions, respectively. The SM parameters: $m_W = 80.377$ GeV, $m_Z = 91.1876$ GeV, $m_t = 172.69$ GeV, $m_h = 125.25$ GeV, and $v_h = 246.22$ GeV [91].

Thermal corrections to the total scalar potential can alter the vacuum structure. For suitable parameter choices, at a critical temperature $T_{c,1}$, the quadratic coefficient of the field ϕ_1, denoted by μ_1^2, may be chosen to be negative. Consequently, below this temperature, the thermal potential $V_T(\phi_1,\phi_2,h,T)$ in Eq. (42) will exhibit two degenerate vacua: one at

$$
\langle\phi_1\rangle=0,\quad \langle\phi_2\rangle=0,\quad \langle h\rangle=0, \qquad (46)
$$

and the other at

$$\langle\phi_1\rangle = \phi_{1,f_1}, \quad \langle\phi_2\rangle = 0, \quad \langle h\rangle = h_{f_1}. \tag{47}$$

For convenience, we briefly denote $(a,\ b,\ c)$ as the vevs of scalar $(\langle\phi_1\rangle = a,\ \langle\phi_2\rangle = b,\ \langle h\rangle = c)$. As the universe further expands and the temperature drops below $T_{c,1}$, the vacuum state $(\phi_{1,f_1},\ 0,\ h_{f_1})$ becomes energetically favorable, and the universe acquires a nonzero probability to transit from the (0,0,0) to $(\phi_{1,f_1},\ 0,\ h_{f_1})$. As the temperature continues to fall, a second critical temperature $T_{c,2}$ is reached, triggering a subsequent phase transition. The potential $V_T(h, \phi_1, \phi_2, T)$ now drives the system from the vacuum $(\phi_{1,f_2},\ 0,\ h_{f_2})$ to a new vacuum $(\phi_{1,f_3},\ 0,\ h_{f_3})$. After undergoing multiple phase transitions, the universe eventually settles into the final vacuum corresponding to the electroweak symmetry breaking phase: $(0,\ 0,\ v_h)$.

The decay rate per unit volume when phase transition occurs is given by Ref. [104]

$$\Gamma(T) \sim T^4 \left(\frac{S_3(T)}{2\pi T}\right)^{3/2} e^{-S_3(T)/T}, \tag{48}$$

where $S_3(T)$ denotes the Euclidean action corresponding to the $O(3)$-symmetric bounce solution. A first-order electroweak phase transition takes place when the vacuum decay rate per Hubble volume becomes of order one, signaling the onset of bubble nucleation from the electroweak-broken vacuum. The temperature at which this nucleation begins is defined as the nucleation temperature T_n, which satisfies the condition $\Gamma(T_n) = H^3(T_n)$, where $H(T)$ is the Hubble parameter at temperature T.

In a radiation-dominated universe, such as during the electroweak phase transition, the nucleation temperature T_n can be estimated by the following relation [105]

$$\frac{S_3(T_n)}{T_n} \simeq 140, \tag{49}$$

which we adopt as the criterion for a FOEWPT. For each chosen free parameter set, the nucleation temperature T_n is computed by numerically solving Eq. (49) using the `Python` package `CosmoTransitions` [106].

The parameter α, which is crucial for determining the strength of the gravitational wave signal, is defined as the ratio of the vacuum energy difference between the false and true vacua to the radiation energy density:

$$\alpha = \frac{1}{g_* \pi^2 T_n^4/30} \left(T \frac{\partial \Delta V_T}{\partial T} - \Delta V_T \right) \Bigg|_{T_n}. \tag{50}$$

Another important parameter, β, characterizing the inverse time scale of the strongly FOEWPT (sFOEWPT), is defined as

$$\frac{\beta}{H(T_n)} = T \frac{d\left(S_3(T)/T\right)}{dT} \Bigg|_{T=T_n}. \tag{51}$$

GWs are primarily generated through two processes: sound waves propagating in the plasma and magnetohydrodynamic (MHD) turbulence [107, 108]. The total energy density spectrum of the GWs can be expressed as a sum of these two contributions:

$$\Omega_{GW} h^2 \simeq \Omega_{sw} h^2 + \Omega_{turb} h^2. \tag{52}$$

The component originating from sound waves is given by [11, 107]:

$$\Omega_{sw} h^2 = 2.65 \times 10^{-6} \left(\frac{H_*}{\beta} \right) \left(\frac{k_v \alpha}{1+\alpha} \right)^2 \left(\frac{100}{g_*} \right)^{1/3} v_w \left(\frac{f}{f_{sw}} \right)^3 \left(\frac{7}{4 + 3(f/f_{sw})^2} \right)^{7/2}, \tag{53}$$

where g_* is the relativistic degrees of freedom at the temperature T_*, $H_*(T)$ the Hubble constant at the temperature T_* is given by

$$H(T_*) = \sqrt{\frac{8\pi G}{3} \times \frac{\pi^2}{30} g_* T_*^4}. \tag{54}$$

And $v_w = 1$ is the bubble expansion velocity, $k_v = \alpha / \left(0.73 + 0.083\sqrt{\alpha} + \alpha\right)$ is the fraction of released energy going to the kinetic energy of the plasma [109]. Here, the temperature $T_* = T_n$. The peak frequency f_{sw} of the energy density spectrum is

$$f_{sw} = 1.9 \times 10^{-5} \frac{1}{v_w} \left(\frac{\beta}{H_*} \right) \left(\frac{T_*}{100\ \text{GeV}} \right) \left(\frac{g_*}{100} \right)^{1/6} \text{Hz}. \tag{55}$$

In addition to sound waves, a fraction of the energy is released via MHD turbulence. The energy density spectrum for this contribution is [11, 110, 111]:

$$\Omega_{turb} h^2 = 3.35 \times 10^{-4} \left(\frac{H_*}{\beta} \right) \left(\frac{k_{turb} \alpha}{1+\alpha} \right)^{3/2} \left(\frac{100}{g_*} \right)^{1/3} v_w \frac{(f/f_{turb})^3}{(1 + (f/f_{turb}))^{11/3} (1 + 8\pi f/h_*)}, \tag{56}$$

where the energy proportion of MHD $k_{turb} = 0.1 k_v$, and the peak frequency of MHD induced GW is given by

$$f_{turb} = 2.7 \times 10^{-5} \frac{1}{v_w} \left(\frac{\beta}{H_*}\right) \left(\frac{T_*}{100\ \text{GeV}}\right) \left(\frac{g_*}{100}\right)^{1/6} \text{Hz}. \tag{57}$$

After getting the energy density spectrum of GWs, the strength of the GW signal detectable by instruments can be quantified using the signal-to-noise ratio (SNR) [112]

$$\text{SNR} = \sqrt{\delta \times \mathcal{J} \int df \left[\frac{h^2\Omega_{GW}(f)}{h^2\Omega_{exp}(f)}\right]^2}, \tag{58}$$

where $\mathcal{J}$ represents the mission duration, and $h^2\Omega_{exp}$ characterizes the sensitivity of the detector, here we choose $\mathcal{J} = 9.46 \times 10^7$s (more than 3 years) [113]. The factor δ arises from the number of independent channels available for cross-correlation between detectors, which is equal to 2 in the case of U-DECIGO [11].

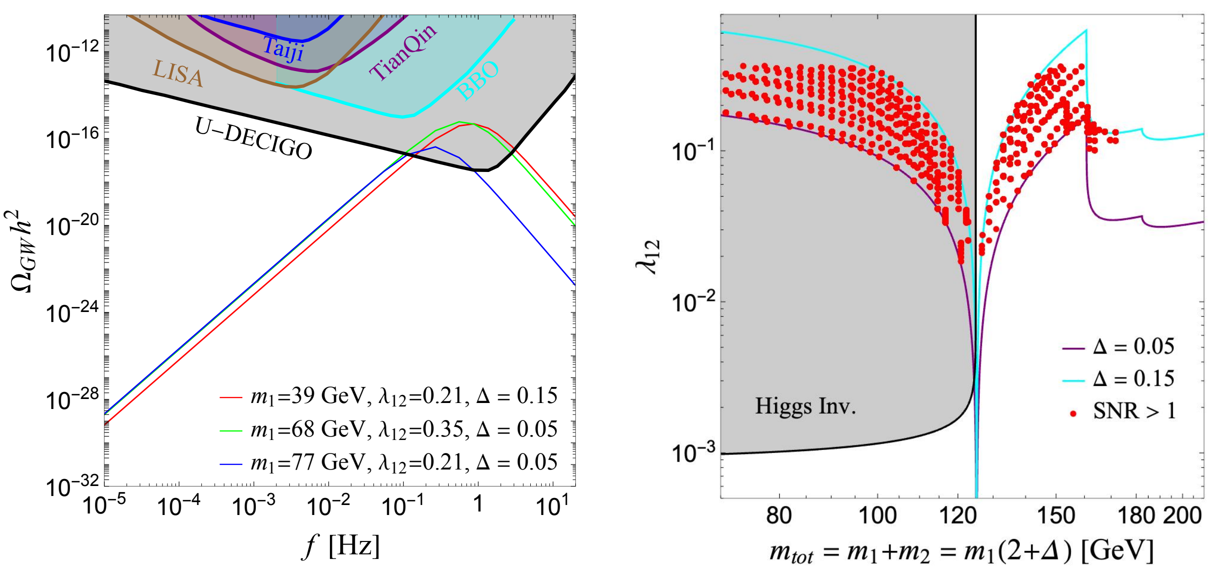

FIG. 3. **Left**: A representative gravitational wave spectrum is shown in comparison with the sensitivity curve of several GW detectors (obtained by scanning over the parameter λ_ϕ to maximize the signal).
Right: Red dots represent regions of parameter space that yield strongly first-order phase transitions with a GW signal-to-noise ratio SNR > 1. The cyan and purple lines indicate regions consistent with relic abundance constraints for $\Delta = 0.15$ and 0.05. The shaded region represents constraints from the Higgs invisible decay.

We then perform simulations by setting $\Delta = 0.05,\ 0.10,\ 0.15$, and scanning λ_{12} within the relic abundance allowed region for $\Delta \in [0.05,\ 0.15]$. The DM mass m_1 is varied from 30 GeV to 90 GeV, and λ_ϕ is scanned from 0.1 to 2.0. The results show that approximately 20% of the parameter points lead to a FOEWPT, and about 2% parameter points yield a strong phase transition with SNR > 1.

The left panel of Fig. 3 shows the GW spectra with the sensitivity curves of present and future gravitational wave experiments, including LISA [114], BBO [115], Taiji [116–118], TianQin [119], and U-DECIGO. It can be seen that, in some cases, the peak frequency of the gravitational wave energy density generated by the phase transition is close to the frequency where the U-DECIGO detector can reach. As to the other GW detectors, comparing their reaches with our predicted GW spectra, we find that their sensitivity ranges do not overlap with the GW frequencies relevant to our study, and thus are not sufficient to detect the predicted signal strengths. Then, combined with Eq. (58), the corresponding SNR can be calculated. We highlight several benchmark points that yield the largest SNR values. Notably, the signal represented by the blue curve can potentially be detected by both gravitational wave detectors and collider experiments, as will be discussed in the next section.

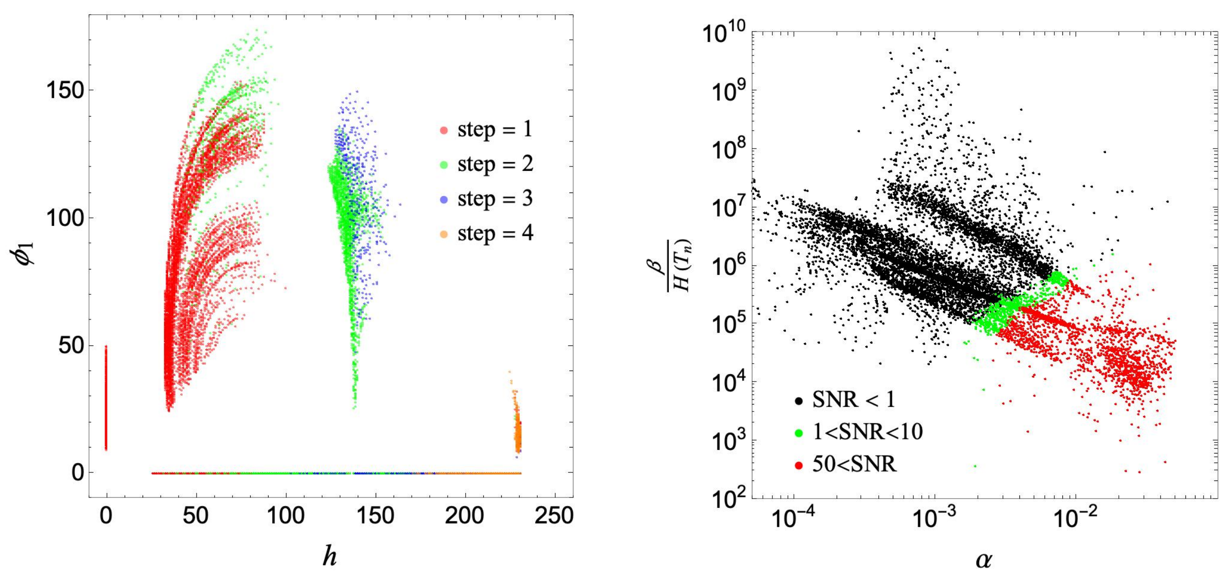

FIG. 4. Final phase points in multi-step phase transitions (left) and the corresponding SNR, α, and $\beta/H(T_n)$ values across different model parameters (right). Red points indicate parameter regions where SNR > 50.

The right panel of Fig. 3 presents the parameter space leading to strongly first-order phase transitions with SNR > 1, indicated by red dots. It can be observed that these points predominantly originate from the mass range $m_1 \in [40, 80]$ GeV. The cyan and purple curves represent the relic abundance for different mass differences. As discussed earlier, $\mu_1^2 < 0$ may lead to a first-order phase transition. From Eq. (24), it can be seen that when λ_{12} becomes too small, $\mu_1^2 > 0$, indicating that no phase transition occurs. The shaded region denotes parameter space excluded by constraints from Higgs invisible decays. They exclude the mass region for $m_{tot} < m_h$.

The left panel of Fig. 4 illustrates the whole multi-step phase transition process. It can be observed that the first-step phase transition predominantly proceeds along the direction of the DM field, ϕ_1. This is because, for $\mu_1^2 < 0$ and $\langle h \rangle = 0$, the vacuum expectation value of ϕ_1 tends to acquire a nonzero value. In contrast, the subsequent transition drives the vacuum expectation value toward the Higgs field axis. Finally, the VEVs of the fields return to the SM case, $\langle h \rangle = v_h$ and $\langle \phi_1 \rangle = 0$. As for the DM partner, ϕ_2, its corresponding phase values always tend to zero and are therefore omitted in this plot. The right panel of Fig. 4 shows the GW SNRs for phase transition parameters α and $\beta/H(T_n)$ calculated from first-order phase transitions for given parameters. The regions (red and green dots) with SNR > 1, which may be detectable by the U-DECIGO GW detector. Simulation results suggest that sFOEWPT primarily arises from the last step of the phase transition.

V. INELASTIC DARK MATTER AT COLLIDERS

In our model, two new particles, ϕ_1 and ϕ_2, are introduced. We require that ϕ_1 and ϕ_2 contribute to the correct relic abundance of DM, support a potential sFOEWPT, and are consistent with existing experimental constraints. These conditions restrict the mass of ϕ_2 to lie within the range $m_2 \in (m_h - m_1, 2m_W - m_1)$. As discussed in Sec. I, ϕ_2 decays into ϕ_1 and SM particles, with its lifetime being sufficiently long due to the small mass difference Δ between ϕ_1 and ϕ_2, combined with phase space suppression. This results in ϕ_2 behaving as a long-lived particle, capable of producing substantial observable signals at pp colliders. Therefore, our focus is on detecting these extended signals from ϕ_2 within the mass range specified earlier at both ongoing and proposed LHC experiments.

Specifically, LLP ϕ_2 may undergo decay subsequent to spatial displacement within the detector, accompanied by a detectable time lag, leading to discernible characteristics distinct from the majority of SM backgrounds. However, to effectively capture and identify these signals, enhancements and specialized apparatus in detectors are imperative. Fortunately, the upcoming HL-LHC upgrade will incorporate precision timing layers that reduce pile-up interference and improve measurements of particle properties, such as position, momentum, and energy. These advancements will be crucial for the exploration of LLPs using tailored detection strategies. Regarding these upgrades, the CMS experiment is developing the Minimum Ionizing Particle (MIP) Timing Detector to achieve these goals [120, 121], ATLAS is working on the High Granularity Timing Detector [122], and LHCb plans to implement similar precision timing upgrades in the near future [123].

As in many DM scenarios, both ϕ_2 and ϕ_1 at colliders typically lead to missing energy, which can be effectively triggered by high-energy monojet events. To efficiently detect LLPs, various strategies are employed. One common approach involves requiring an initial-state radiation (ISR) jet alongside the signal process, which helps identify the primary interaction point [124]. A high transverse momentum ISR jet with $p_T^j > 120$ GeV is typically used to trigger the Jet+MET strategy efficiently [125]. Additionally, there have been proposals to include displaced track information in the Level-1 (L1) hardware trigger, with minimum thresholds for track transverse momentum as low as $p_T^j \sim 2$ GeV [126]. While using high-energy ISR jets as a trigger mechanism is a cautious approach, there is still room for further refinement. By combining specific signal selection criteria, the behavior of LLPs can be thoroughly explored at the colliders. Moreover, the presence of leptons in the final state can significantly relax the triggering conditions compared to purely hadronic scenarios. To explore LLP ϕ_2, two promising search methods are adopted: the displaced muon-jet (DMJ) method [68] and the time-delayed method (TDM) [70, 124].

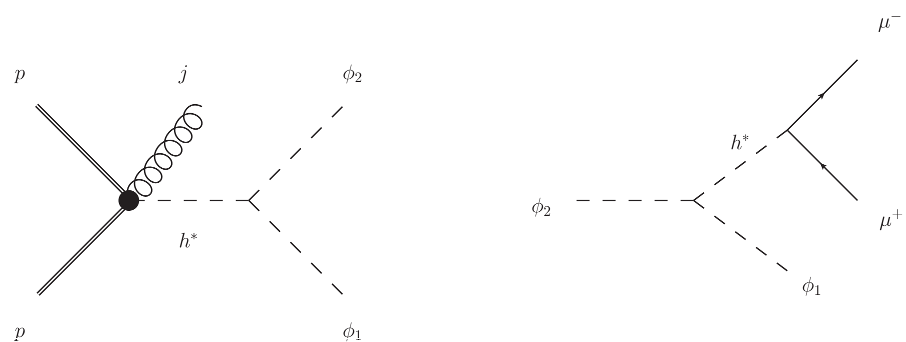

FIG. 5. Feynman diagrams for productions and decays of DM partner ϕ_2 at the HL-LHC.

In our study, we will consider the associated production of ϕ_2 with an ISR high-p_T jet, followed by the decay of ϕ_2 to ϕ_1 and a pair of muons, as shown in Fig. 5. The full process is described by:

$$pp \to jh^* \to j\phi_2\phi_1, \phi_2 \to \phi_1\mu^+\mu^-, \tag{59}$$

where h^* represents the off-shell Higgs since we focus on the region $(m_1 + m_2 > m_h)$ relevant for the DM and its partner mass regions of interest. The corresponding Feynman diagrams are shown in Fig. 5. For simplicity, we focus on the muon decay channel, which, though subdominant, is easily detectable at pp colliders.

A. Displaced Muon-Jet Method

For the DMJ method, in addition to the stringent ISR jet requirement of $p_T^j > 120$ GeV, the decay products of ϕ_2 typically exhibit low momenta due to the small mass difference between ϕ_1 and ϕ_2. To identify muons originating from ϕ_2 decays, we impose that each muon has a transverse momentum $p_T^\mu > 5$ GeV [127]. Furthermore, for accurate reconstruction of their trajectories, these muons must pass through multiple layers of the tracking system, which is ensured by requiring that the radial displacement of the ϕ_2 decay vertex does not exceed 30 cm. To mitigate the impact of SM backgrounds, a common practice is to require a substantial displacement of muon tracks. Specifically, we impose a transverse impact parameter of $d_0^\mu > 1$ mm [68]. Thus, the comprehensive selection criteria for the DMJ method are:

$$\text{DMJ:} \quad p_T^j > 120\text{ GeV}, \quad p_T^\mu > 5\text{ GeV}, \quad r_{\phi_2} < 30\text{ cm}, \quad d_0^\mu > 1\text{ mm}, \tag{60}$$

where r_{ϕ_2} denotes the radial displacement of the ϕ_2 decay vertex. As described in Ref. [68], these selection criteria are successful in significantly reducing background processes to a negligible extent for an integrated luminosity of HL-LHC, $\mathcal{L} = 3\text{ ab}^{-1}$.

B. Time-Delayed Method

For the TDM, the key feature is the slow movement of the long-lived, heavy particle, which leads to a noticeable time delay compared to SM processes. In the SM, particles like mesons and leptons move close to the speed of light, while heavy particles such as gauge bosons and the Higgs boson decay rapidly into lighter particles, causing minimal time delays. However, with heavy new particles beyond the SM, significant time delays occur due to their slower speeds. The time delay, Δt_μ, for the decay process $\phi_2 \to \phi_1 \mu^+ \mu^-$ is given by [124]:

$$\Delta t_\mu = \frac{L_{\phi_2}}{\beta_{\phi_2}} + \frac{L_\mu}{\beta_\mu} - \frac{L_{\text{SM}}}{\beta_{\text{SM}}}, \tag{61}$$

where L and β represent the propagation distance and velocity of each particle, respectively. For simplicity, we assume the trajectories of ϕ_2 and its decay products are straight lines, and $\beta_\mu = \beta_{\rm SM} = 1$. Since particles like b quarks and τ leptons decay quickly into lighter, highly relativistic particles, these assumptions hold true. The selection criteria for the TDM are:

$$\begin{aligned} \text{TDM:} \quad & p_T^j > 120\ \text{GeV}\ (30\ \text{GeV}), \quad p_T^\mu > 3\ \text{GeV}, \quad |\eta| < 2.4, \\ & \Delta t_\mu > 0.3\ \text{ns}, \quad 5\ \text{cm} < r_{\phi_2} < 1.17\ \text{m}, \quad z_{\phi_2} < 3.04\ \text{m}, \end{aligned} \tag{62}$$

where η is the pseudorapidity of the jets and muons, and Δt_μ is the measured time delay of the muon. The decay position requirements, r_{ϕ_2} and z_{ϕ_2}, ensure that the decay products leave hits within the CMS MIP Timing Detector. We also evaluate two thresholds for ISR jet transverse momentum: a conservative requirement of $p_T^j > 120$ GeV and a more optimistic scenario with $p_T^j > 30$ GeV, which becomes feasible due to the additional timing and lepton information. Under these conditions, SM background contamination can be neglected.

Using the above two methods, we can explore a dedicated search for the LLP ϕ_2. The number of signal events arising from ϕ_2 decays that satisfy the selection criteria is given by:

$$N_{\rm sig}^{\mu\mu} = \mathcal{L} \cdot \sigma_{\rm sig} \cdot P(\phi_2) \cdot \epsilon_{\rm cut}, \tag{63}$$

where $P(\phi_2)$ is the probability that ϕ_2 decays while satisfying the specific geometric cuts, $\mathcal{L} = 3\ \text{ab}^{-1}$ is the integrated luminosity of the HL-LHC, and $\epsilon_{\rm cut}$ is the efficiency of the remaining kinematic selection criteria. To accurately determine the signal yield, a parton-level Monte Carlo simulation is performed using `MadGraph5_aMC@NLO` with the UFO model created by `FeynRules` [128]. This simulation samples the decay times of ϕ_2 for each specific proper lifetime, and the displacement parameters r_{ϕ_2} and d_0^μ (or Δt_μ, r_{ϕ_2} for DMJ and TDM, respectively) are derived from the kinematics of ϕ_2 and its decay products. Finally, the efficiency $\epsilon_{\rm cut}$ is calculated via event-by-event analysis.

Based on the analysis of cut efficiency for the DMJ and TDM, we can estimate the sensitivities for the DM partner, ϕ_2, at HL-LHC, with a center-of-mass energy of $\sqrt{s} = 14$ TeV and an integrated luminosity of $\mathcal{L} = 3\ \text{ab}^{-1}$. Unfortunately, the sensitivity of the TDM is too low to probe the relevant parameter space for $\Delta = 0.05$ (0.07) in the mass range $m_{tot} \in [m_h, 200]$ ($[m_h, 158]$) GeV and $\lambda_{12} \in [6 \times 10^{-3}, 17]$ ($[0.014, 3]$). This limitation arises from the highly boosted nature of ϕ_2, which results from its small mass and high kinematic energy. Consequently, the time delay

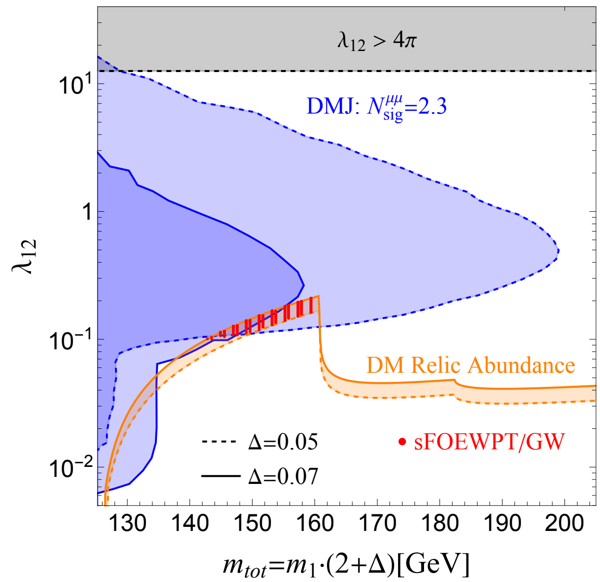

FIG. 6. Expected sensitivities at the future HL-LHC to the scalar iDM model in the parameter space determined by λ_{12} and $m_{\rm tot} = m_1 + m_2 = m_1 \cdot (2 + \Delta)$, with an integrated luminosity of $\mathcal{L} = 3$ ab^{-1} and a center-of-mass energy of $\sqrt{s} = 14$ TeV, where the mass splitting $\Delta = 0.05$ (dashed) and 0.07 (solid). The projected sensitivity for the displaced muon-jets method with 2.3 signals is depicted by the blue dashed (solid) contour lines. The dashed (solid) orange line and the orange-shaded region depict the parameter space consistent with the observed Dark Matter relic abundance for $\Delta = 0.05$ ($\Delta = 0.07$) and Δ ranging from 0.05 to 0.07. The red points labeled "sFOEWPT/GW" within this orange-shaded area highlight the regions of strongly FOEWPT with GWs to be explored in forthcoming GW observatories for $\Delta \in [0.05, 0.07]$. Additionally, the gray-shaded region identifies areas where λ_{12} surpasses 4π.

required for the TDM method to be effective is not prominent, making this approach less viable for the given parameter space. Additionally, the small mass difference between ϕ_1 and ϕ_2 leads to soft muons from ϕ_2 decays, which complicates the application of the TDM selection criteria.

In contrast, the DMJ method demonstrates significant sensitivity for $\Delta = 0.05$ (0.07) in the mass range $m_{tot} \in [m_h, 200]$ ($[m_h, 158]$) GeV and $\lambda_{12} \in [6\times10^{-3}, 17]$ ($[0.014, 3]$). As shown in Fig. 6, the LLP sensitivity of the DMJ method decreases with increasing mass of ϕ_2. This indicates that the DMJ method is especially effective for relatively lighter DM partners, where the decay products of ϕ_2 can be more easily detected through distinct kinematic signatures. This decline is due to two key factors: a reduced production cross-section, $\sigma(pp \to j\phi_2\phi_1)$, and a diminished branching ratio, $Br(\phi_2 \to \phi_1\mu^+\mu^-)$, both of which decrease as the mass of ϕ_2 increases.

Moreover, it is clear that the sensitivity for $\Delta = 0.07$ is considerably weaker than for $\Delta = 0.05$, despite the relatively small difference of 0.02. This disparity is a consequence of the fifth-power dependence of the total decay width of ϕ_2 on Δ, meaning that even a minor increase in Δ can lead to a significant increase in the total decay width. As a result, in order to satisfy the long-lived requirement of the DMJ approach, the coupling parameter λ_{12} must be substantially reduced. However, this reduction also diminishes the production cross-section of $pp \to j\phi_1\phi_2$. Therefore, weaker sensitivity is observed for larger mass splitting ratios. Additionally, the branching ratio of $\phi_2 \to \phi_1\mu^+\mu^-$ decreases for larger Δ, further impeding the sensitivity of the DMJ method.

Fig. 6 also highlights regions of parameter space that are consistent with the correct DM relic abundance and sFOEWPT. The solid and dashed orange lines represent the boundaries for the correct DM relic abundance for $\Delta = 0.07$ and 0.05, respectively. The red points, labeled "sFOEWPT/GW", indicate sFOEWPT regions that are detectable through GWs, which lie within the correct DM relic abundance parameter space for $\Delta \in [0.05, 0.07]$. Furthermore, the gray-shaded area identifies regions where the coupling parameter λ_{12} exceeds the theoretical limit of 4π, making the model non-perturbative. Notably, the parameter space in the mass range $m_{tot} \in [142, 155]$ GeV and $\lambda_{12} \in [0.1, 0.2]$ offers a promising opportunity for joint exploration of the iDM model, combining both gravitational wave observations and collider searches.

VI. CONCLUSIONS

The iDM mechanism provides an elegant way to evade stringent direct-detection limits and has attracted growing interest in recent years. While fermionic iDM models have been extensively explored, scalar iDM offers equally rich phenomenology. In this work, we proposed and studied a purely inelastic scalar DM model in which two scalar states-the DM particle ϕ_1 and its excited partner ϕ_2-interact inelastically with the SM through a Higgs portal. After diagonalizing the mass matrix, only inelastic couplings among ϕ_1, ϕ_2, and the Higgs remain. This setup naturally explains the observed DM relic abundance via thermal coannihilation, predicts a strongly FOEWPT in the early universe capable of generating detectable GWs, and produces long-lived ϕ_2 signatures at colliders due to the small ϕ_1–ϕ_2 mass splitting and the off-shell Higgs mediator.

Crucially, we find out a particularly compelling parameter region, $m_{tot} \in [142, 155]$ GeV and $\lambda_{12} \in [0.1, 0.2]$, where three experimental frontiers converge. In this region, the correct DM relic density is achieved, a sFOEWPT generates GWs detectable by future observatories, and LLP signatures are within the reach of the HL-LHC. This overlap provides a unique opportunity to cross-validate the model through complementary probes from cosmology, astrophysics, and collider physics, highlighting the power of a multi-frontier approach in the search for iDM.

VII. ACKNOWLEDGMENTS

The work of J.G is supported by the Postdoctoral Fellowship Program (Grade C) of China Postdoctoral Science Foundation under Grant No. GZC20252775. The work of J.L. is supported by the National Science Foundation of China under Grant No. 12235001 and No. 12475103. The work of X.P.W. is supported by National Science Foundation of China under Grant No. 12375095, and the Fundamental Research Funds for the Central Universities. J.L. and X.P.W. thank the Asia Pacific Center for Theoretical Physics (APCTP), Pohang, Korea, for their hospitality during the focus program [APCTP-2025-F01], from which this work greatly benefited. J.L. and X.P.W. also thank the Mainz Institute for Theoretical Physics (MITP) of the PRISMA+ Cluster of Excellence (Project ID 390831469) for its hospitality and partial support during the completion of this work. We also acknowledge with appreciation the valuable discussions and insights provided by the members of the Collaboration of Precision Testing and New Physics.

---

[1] **ATLAS** Collaboration, G. Aad et al., *Observation of a new particle in the search for the Standard Model Higgs boson with the ATLAS detector at the LHC*, Phys. Lett. B **716** (2012) 1–29, [arXiv:1207.7214].

[2] **CMS** Collaboration, S. Chatrchyan et al., *Observation of a New Boson at a Mass of 125 GeV with the CMS Experiment at the LHC*, Phys. Lett. B **716** (2012) 30–61, [arXiv:1207.7235].

[3] K. Kajantie, M. Laine, K. Rummukainen, and M. E. Shaposhnikov, *A Nonperturbative analysis of the finite T phase transition in SU(2) x U(1) electroweak theory*, Nucl. Phys. B **493** (1997) 413–438, [hep-lat/9612006].

[4] K. Rummukainen, M. Tsypin, K. Kajantie, M. Laine, and M. E. Shaposhnikov, *The Universality class of the electroweak theory*, Nucl. Phys. B **532** (1998) 283–314, [hep-lat/9805013].

[5] M. Laine and K. Rummukainen, *What's new with the electroweak phase transition?*, Nucl. Phys. B Proc. Suppl. **73** (1999) 180–185, [hep-lat/9809045].

[6] S. Profumo, M. J. Ramsey-Musolf, and G. Shaughnessy, *Singlet Higgs phenomenology and the electroweak phase transition*, JHEP **08** (2007) 010, [arXiv:0705.2425].

[7] J. R. Espinosa, T. Konstandin, and F. Riva, *Strong Electroweak Phase Transitions in the Standard Model with a Singlet*, Nucl. Phys. B **854** (2012) 592–630, [arXiv:1107.5441].

[8] J. M. Cline and K. Kainulainen, *Electroweak baryogenesis and dark matter from a singlet Higgs*, JCAP **01** (2013) 012, [arXiv:1210.4196].

[9] T. Alanne, K. Tuominen, and V. Vaskonen, *Strong phase transition, dark matter and vacuum stability from simple hidden sectors*, Nucl. Phys. B **889** (2014) 692–711, [arXiv:1407.0688].

[10] S. Profumo, M. J. Ramsey-Musolf, C. L. Wainwright, and P. Winslow, *Singlet-catalyzed electroweak phase transitions and precision Higgs boson studies*, Phys. Rev. D **91** (2015), no. 3 035018, [arXiv:1407.5342].

[11] A. Alves, T. Ghosh, H.-K. Guo, K. Sinha, and D. Vagie, *Collider and Gravitational Wave Complementarity in Exploring the Singlet Extension of the Standard Model*, JHEP **04** (2019) 052, [arXiv:1812.09333].

[12] V. Vaskonen, *Electroweak baryogenesis and gravitational waves from a real scalar singlet*, Phys. Rev. D **95** (2017), no. 12 123515, [arXiv:1611.02073].

[13] F. P. Huang, Z. Qian, and M. Zhang, *Exploring dynamical CP violation induced baryogenesis by gravitational waves and colliders*, Phys. Rev. D **98** (2018), no. 1 015014, [arXiv:1804.06813].

[14] W. Cheng and L. Bian, *From inflation to cosmological electroweak phase transition with a complex scalar singlet*, Phys. Rev. D **98** (2018), no. 2 023524, [arXiv:1801.00662].

[15] T. Alanne, T. Hugle, M. Platscher, and K. Schmitz, *A fresh look at the gravitational-wave signal from cosmological phase transitions*, JHEP **03** (2020) 004, [arXiv:1909.11356].

[16] O. Gould, J. Kozaczuk, L. Niemi, M. J. Ramsey-Musolf, T. V. I. Tenkanen, and D. J. Weir, *Nonperturbative analysis of the gravitational waves from a first-order electroweak phase transition*, Phys. Rev. D **100** (2019), no. 11 115024, [arXiv:1903.11604].

[17] M. Carena, Z. Liu, and Y. Wang, *Electroweak phase transition with spontaneous Z_2-breaking*, JHEP **08** (2020) 107, [arXiv:1911.10206].

[18] K. Ghorbani and P. H. Ghorbani, *Strongly First-Order Phase Transition in Real Singlet Scalar Dark Matter Model*, J. Phys. G **47** (2020), no. 1 015201, [arXiv:1804.05798].

[19] P. H. Ghorbani, *Electroweak Baryogenesis and Dark Matter via a Pseudoscalar vs. Scalar*, JHEP **08** (2017) 058, [arXiv:1703.06506].

[20] G. C. Dorsch, S. J. Huber, and J. M. No, *A strong electroweak phase transition in the 2HDM after LHC8*, JHEP **10** (2013) 029, [arXiv:1305.6610].

[21] W. Chao and M. J. Ramsey-Musolf, *Catalysis of Electroweak Baryogenesis via Fermionic Higgs Portal Dark Matter*, arXiv:1503.00028.

[22] P. Basler, M. Krause, M. Muhlleitner, J. Wittbrodt, and A. Wlotzka, *Strong First Order Electroweak Phase Transition in the CP-Conserving 2HDM Revisited*, JHEP **02** (2017) 121, [arXiv:1612.04086].

[23] A. Haarr, A. Kvellestad, and T. C. Petersen, *Disfavouring Electroweak Baryogenesis and a hidden Higgs in a CP-violating Two-Higgs-Doublet Model*, arXiv:1611.05757.

[24] G. C. Dorsch, S. J. Huber, K. Mimasu, and J. M. No, *The Higgs Vacuum Uplifted: Revisiting the Electroweak Phase Transition with a Second Higgs Doublet*, JHEP **12** (2017) 086, [arXiv:1705.09186].

[25] J. O. Andersen, T. Gorda, A. Helset, L. Niemi, T. V. I. Tenkanen, A. Tranberg, A. Vuorinen, and D. J. Weir, *Nonperturbative Analysis of the Electroweak Phase Transition in the Two Higgs Doublet Model*, Phys. Rev. Lett. **121** (2018), no. 19 191802, [arXiv:1711.09849].

[26] J. Bernon, L. Bian, and Y. Jiang, *A new insight into the phase transition in the early Universe with two Higgs doublets*, JHEP **05** (2018) 151, [arXiv:1712.08430].

[27] L. Wang, J. M. Yang, M. Zhang, and Y. Zhang, *Revisiting lepton-specific 2HDM in light of muon* $g-2$ *anomaly*, Phys. Lett. B **788** (2019) 519–529, [arXiv:1809.05857].

[28] X. Wang, F. P. Huang, and X. Zhang, *Gravitational wave and collider signals in complex two-Higgs doublet model with dynamical CP-violation at finite temperature*, Phys. Rev. D **101** (2020), no. 1 015015, [arXiv:1909.02978].

[29] K. Kainulainen, V. Keus, L. Niemi, K. Rummukainen, T. V. I. Tenkanen, and V. Vaskonen, *On the validity of perturbative studies of the electroweak phase transition in the Two Higgs Doublet model*, JHEP **06** (2019) 075, [arXiv:1904.01329].

[30] W. Su, A. G. Williams, and M. Zhang, *Strong first order electroweak phase transition in 2HDM confronting future Z & Higgs factories*, JHEP **04** (2021) 219, [arXiv:2011.04540].

[31] D. E. Morrissey and M. J. Ramsey-Musolf, *Electroweak baryogenesis*, New J. Phys. **14** (2012) 125003, [arXiv:1206.2942].

[32] J. M. Cline, *Baryogenesis*, in Les Houches Summer School - Session 86: Particle Physics and Cosmology: The Fabric of Spacetime, 9, 2006. hep-ph/0609145.

[33] M. Trodden, *Electroweak baryogenesis*, Rev. Mod. Phys. **71** (1999) 1463–1500, [hep-ph/9803479].

[34] L. Roszkowski, E. M. Sessolo, and S. Trojanowski, *WIMP dark matter candidates and searches—current status and future prospects*, Rept. Prog. Phys. **81** (2018), no. 6 066201, [arXiv:1707.06277].

[35] **Planck** Collaboration, N. Aghanim et al., *Planck 2018 results. VI. Cosmological parameters*, Astron. Astrophys. **641** (2020) A6, [arXiv:1807.06209]. [Erratum: Astron.Astrophys. 652, C4 (2021)].

[36] **Particle Data Group** Collaboration, K. A. Olive et al., *Review of Particle Physics*, Chin. Phys. C **38** (2014) 090001.

[37] **XENON** Collaboration, E. Aprile et al., *Dark Matter Search Results from a One Ton-Year Exposure of XENON1T*, Phys. Rev. Lett. **121** (2018), no. 11 111302, [arXiv:1805.12562].

[38] **CDEX** Collaboration, Z. Z. Liu et al., *Constraints on Spin-Independent Nucleus Scattering with sub-GeV Weakly Interacting Massive Particle Dark Matter from the CDEX-1B Experiment at the China Jinping Underground Laboratory*, Phys. Rev. Lett. **123** (2019), no. 16 161301, [arXiv:1905.00354].

[39] **LUX** Collaboration, D. S. Akerib et al., *Results from a search for dark matter in the complete LUX exposure*, Phys. Rev. Lett. **118** (2017), no. 2 021303, [arXiv:1608.07648].

[40] **PandaX-4T** Collaboration, Y. Meng et al., *Dark Matter Search Results from the PandaX-4T Commissioning Run*, Phys. Rev. Lett. **127** (2021), no. 26 261802, [arXiv:2107.13438].

[41] **PandaX-II** Collaboration, X. Cui et al., *Dark Matter Results From 54-Ton-Day Exposure of PandaX-II Experiment*, Phys. Rev. Lett. **119** (2017), no. 18 181302, [arXiv:1708.06917].

[42] **LZ** Collaboration, J. Aalbers et al., *First Dark Matter Search Results from the LUX-ZEPLIN (LZ) Experiment*, Phys. Rev. Lett. **131** (2023), no. 4 041002, [arXiv:2207.03764].

[43] **AMS** Collaboration, M. Aguilar et al., *Electron and Positron Fluxes in Primary Cosmic Rays Measured with the Alpha Magnetic Spectrometer on the International Space Station*, Phys. Rev. Lett. **113** (2014) 121102.

[44] **Fermi-LAT** Collaboration, M. Ackermann et al., *Dark Matter Constraints from Observations of 25 Milky Way Satellite Galaxies with the Fermi Large Area Telescope*, Phys. Rev. D **89** (2014) 042001, [arXiv:1310.0828].

[45] **DAMPE** Collaboration, G. Ambrosi et al., *Direct detection of a break in the teraelectronvolt cosmic-ray spectrum of electrons and positrons*, Nature **552** (2017) 63–66, [arXiv:1711.10981].

[46] **AMS** Collaboration, L. Accardo et al., *High Statistics Measurement of the Positron Fraction in Primary Cosmic Rays of 0.5–500 GeV with the Alpha Magnetic Spectrometer on the International Space Station*, Phys. Rev. Lett. **113** (2014) 121101.

[47] **Fermi-LAT** Collaboration, M. Ackermann et al., *Searching for Dark Matter Annihilation from Milky Way Dwarf Spheroidal Galaxies with Six Years of Fermi Large Area Telescope Data*, Phys. Rev. Lett. **115** (2015), no. 23 231301, [arXiv:1503.02641].

[48] **Fermi-LAT, DES** Collaboration, A. Albert et al., *Searching for Dark Matter Annihilation in Recently Discovered Milky Way Satellites with Fermi-LAT*, Astrophys. J. **834** (2017), no. 2 110, [arXiv:1611.03184].

[49] **Super-Kamiokande** Collaboration, S. Desai et al., *Search for dark matter WIMPs using upward through-going muons in Super-Kamiokande*, Phys. Rev. D **70** (2004) 083523, [hep-ex/0404025]. [Erratum: Phys.Rev.D 70, 109901 (2004)].

[50] **Super-Kamiokande** Collaboration, T. Tanaka et al., *An Indirect Search for WIMPs in the Sun using 3109.6 days of upward-going muons in Super-Kamiokande*, Astrophys. J. **742** (2011) 78, [arXiv:1108.3384].

[51] J. Abdallah et al., *Simplified Models for Dark Matter Searches at the LHC*, Phys. Dark Univ. **9-10** (2015) 8–23, [arXiv:1506.03116].

[52] D. Abercrombie et al., *Dark Matter benchmark models for early LHC Run-2 Searches: Report of the ATLAS/CMS Dark Matter Forum*, Phys. Dark Univ. **27** (2020) 100371, [arXiv:1507.00966].

[53] G. Krnjaic, *Probing Light Thermal Dark-Matter With a Higgs Portal Mediator*, Phys. Rev. D **94** (2016), no. 7 073009, [arXiv:1512.04119].

[54] A. Boveia and C. Doglioni, *Dark Matter Searches at Colliders*, Ann. Rev. Nucl. Part. Sci. **68** (2018) 429–459, [arXiv:1810.12238].

[55] G. Arcadi, A. Djouadi, and M. Raidal, *Dark Matter through the Higgs portal*, Phys. Rept. **842** (2020) 1–180, [arXiv:1903.03616].

[56] **ATLAS** Collaboration, *A search for dark matter produced in association with a dark Higgs boson decaying into a Higgs boson pair in 3b or 4b final states using pp collisions at* $\sqrt{s} = 13$ *TeV with the ATLAS detector*, arXiv:2507.02175.

[57] M. V. Pokidova, Y. G. Naryshkin, and Y. A. Berdnikov, *Searches for Higgs Boson Decays into Dark Matter Particles in the ATLAS Experiment*, Phys. Part. Nucl. **56** (2025), no. 3 809–813.

[58] **CMS** Collaboration, M. Wassmer, *Searches for dark matter with CMS*, PoS **ICHEP2024** (2025) 732.

[59] K. Griest and D. Seckel, *Three exceptions in the calculation of relic abundances*, Phys. Rev. D **43** (1991) 3191–3203.

[60] M. J. Baker et al., *The Coannihilation Codex*, JHEP **12** (2015) 120, [arXiv:1510.03434].

[61] D. Tucker-Smith and N. Weiner, *Inelastic dark matter*, Phys. Rev. D **64** (2001) 043502, [hep-ph/0101138].

[62] D. Tucker-Smith and N. Weiner, *The Status of inelastic dark matter*, Phys. Rev. D **72** (2005) 063509, [hep-ph/0402065].

[63] G. Dalla Valle Garcia, *A minimalistic model for inelastic dark matter*, Phys. Lett. B **862** (2025) 139320, [arXiv:2411.02147].

[64] I. V. Voronchikhin and D. V. Kirpichnikov, *Examining scalar portal inelastic dark matter with lepton fixed target experiments*, arXiv:2505.04290.

[65] J.-J. Zhang, Z.-L. Han, A. Liu, and F.-L. Shao, *Inelastic Dirac dark matter in U(1)B−L*, Nucl. Phys. B **1014** (2025) 116864, [arXiv:2411.06744].

[66] A. Berlin, G. Krnjaic, and E. Pinetti, *Reviving MeV-GeV indirect detection with inelastic dark matter*, Phys. Rev. D **110** (2024), no. 3 035015, [arXiv:2311.00032].

[67] C.-T. Lu, J. Tu, and L. Wu, *Probing inelastic dark matter at the LHC, FASER, and STCF*, Phys. Rev. D **109** (2024), no. 1 015018, [arXiv:2309.00271].

[68] E. Izaguirre, G. Krnjaic, and B. Shuve, *Discovering Inelastic Thermal-Relic Dark Matter at Colliders*, Phys. Rev. D **93** (2016), no. 6 063523, [arXiv:1508.03050].

[69] F. D'Eramo, K. Hambleton, S. Profumo, and T. Stefaniak, *Dark matter inelastic up-scattering with the interstellar plasma: A new source of x-ray lines, including at 3.5 keV*, Phys. Rev. D **93** (2016), no. 10 103011, [arXiv:1603.04859].

[70] A. Berlin and F. Kling, *Inelastic Dark Matter at the LHC Lifetime Frontier: ATLAS, CMS, LHCb, CODEX-b, FASER, and MATHUSLA*, Phys. Rev. D **99** (2019), no. 1 015021, [arXiv:1810.01879].

[71] N. Okada and O. Seto, *Inelastic extra $U(1)$ charged scalar dark matter*, Phys. Rev. D **101** (2020), no. 2 023522, [arXiv:1908.09277].

[72] D. W. Kang, P. Ko, and C.-T. Lu, *Exploring properties of long-lived particles in inelastic dark matter models at Belle II*, JHEP **04** (2021) 269, [arXiv:2101.02503].

[73] N. F. Bell, J. B. Dent, B. Dutta, S. Ghosh, J. Kumar, and J. L. Newstead, *Low-mass inelastic dark matter direct detection via the Migdal effect*, Phys. Rev. D **104** (2021), no. 7 076013, [arXiv:2103.05890].

[74] B. Batell, J. Berger, L. Darmé, and C. Frugiuele, *Inelastic dark matter at the Fermilab Short Baseline Neutrino Program*, Phys. Rev. D **104** (2021), no. 7 075026, [arXiv:2106.04584].

[75] N. F. Bell, J. B. Dent, B. Dutta, S. Ghosh, J. Kumar, J. L. Newstead, and I. M. Shoemaker, *Cosmic-ray upscattered inelastic dark matter*, Phys. Rev. D **104** (2021) 076020, [arXiv:2108.00583].

[76] J. Li, T. Nomura, and T. Shimomura, *Inelastic dark matter from dark Higgs boson decays at FASER*, JHEP **09** (2022) 140, [arXiv:2112.12432].

[77] A. Filimonova, S. Junius, L. Lopez Honorez, and S. Westhoff, *Inelastic Dirac dark matter*, JHEP **06** (2022) 048, [arXiv:2201.08409].

[78] E. Bertuzzo, A. Scaffidi, and M. Taoso, *Searching for inelastic dark matter with future LHC experiments*, JHEP **08** (2022) 100, [arXiv:2201.12253].

[79] T. R. Slatyer, *Indirect dark matter signatures in the cosmic dark ages. I. Generalizing the bound on s-wave dark matter annihilation from Planck results*, Phys. Rev. D **93** (2016), no. 2 023527, [arXiv:1506.03811].

[80] G. D. V. Garcia, F. Kahlhoefer, M. Ovchynnikov, and T. Schwetz, *Not-so-inelastic Dark Matter*, JHEP **02** (2025) 127, [arXiv:2405.08081].

[81] G. Krnjaic, D. Rocha, and I. R. Wang, *Discovering Dark Matter with the MUonE Experiment*, Phys. Rev. Lett. **134** (2025), no. 16 161801, [arXiv:2409.00170].

[82] N. Okada and O. Seto, *Discovery potential of a long-lived partner of inelastic dark matter at MATHUSLA in $U(1)_{X_3}$ extension of the standard model*, arXiv:2409.12754.

[83] W. Liu and J. Sun, *Lepton collider imprints of an inelastic dark matter model*, Phys. Rev. D **111** (2025), no. 11 115022, [arXiv:2503.21083].

[84] J. Guo, Y. He, J. Liu, and X.-P. Wang, *Heavy long-lived coannihilation partner from inelastic Dark Matter model and its signatures at the LHC*, JHEP **04** (2022) 024, [arXiv:2111.01164].

[85] D. Hooper, G. Krnjaic, D. Rocha, and S. Roy, *Gamma-Rays and Gravitational Waves from Inelastic Higgs Portal Dark Matter*, arXiv:2507.22975.

[86] S. Mirzaie, K. Ghorbani, and P. Ghorbani, *Fermion Dark Matter Effect on Electroweak Phase Transition*, arXiv:2502.04265.

[87] J. Alimena et al., *Searching for long-lived particles beyond the Standard Model at the Large Hadron Collider*, J. Phys. G **47** (2020), no. 9 090501, [arXiv:1903.04497].

[88] B. Grinstein, L. J. Hall, and L. Randall, *Do B meson decays exclude a light Higgs?*, Phys. Lett. B **211** (1988) 363–369.

[89] M. W. Winkler, *Decay and detection of a light scalar boson mixing with the Higgs boson*, Phys. Rev. D **99** (2019), no. 1 015018, [arXiv:1809.01876].

[90] K. Griest and D. Seckel, *Three exceptions in the calculation of relic abundances*, Phys. Rev. D **43** (May, 1991) 3191–3203.

[91] **Particle Data Group** Collaboration, S. Navas et al., *Review of particle physics*, Phys. Rev. D **110** (2024), no. 3 030001.

[92] J. A. Casas, D. G. Cerdeño, J. M. Moreno, and J. Quilis, *Reopening the Higgs portal for single scalar dark matter*, JHEP **05** (2017) 036, [arXiv:1701.08134].

[93] C. Armand and B. Herrmann, *Dark matter indirect detection limits from complete annihilation patterns*, JCAP **11** (2022) 055, [arXiv:2210.01220].

[94] P. J. Fox, R. Harnik, J. Kopp, and Y. Tsai, *Missing Energy Signatures of Dark Matter at the LHC*, Phys. Rev. D **85** (2012) 056011, [arXiv:1109.4398].

[95] J. Claude, M. Dutra, and S. Godfrey, *Probing feebly interacting dark matter with monojet searches*, Phys. Rev. D **107** (2023), no. 7 075006, [arXiv:2208.09422].

[96] **ATLAS** Collaboration, G. Aad et al., *Search for new phenomena in events with an energetic jet and missing transverse momentum in pp collisions at* $\sqrt{s}$ *=13 TeV with the ATLAS detector*, Phys. Rev. D **103** (2021), no. 11 112006, [arXiv:2102.10874].

[97] **CMS** Collaboration, A. Tumasyan et al., *Search for new particles in events with energetic jets and large missing transverse momentum in proton-proton collisions at* $\sqrt{s}$ *= 13 TeV*, JHEP **11** (2021) 153, [arXiv:2107.13021].

[98] **CMS** Collaboration, A. Tumasyan et al., *Search for invisible decays of the Higgs boson produced via vector boson fusion in proton-proton collisions at s=13 TeV*, Phys. Rev. D **105** (2022), no. 9 092007, [arXiv:2201.11585].

[99] R. Frederix, S. Frixione, V. Hirschi, D. Pagani, H. S. Shao, and M. Zaro, *The automation of next-to-leading order electroweak calculations*, JHEP **07** (2018) 185, [arXiv:1804.10017]. [Erratum: JHEP 11, 085 (2021)].

[100] J. Alwall, R. Frederix, S. Frixione, V. Hirschi, F. Maltoni, O. Mattelaer, H. S. Shao, T. Stelzer, P. Torrielli, and M. Zaro, *The automated computation of tree-level and next-to-leading order differential cross sections, and their matching to parton shower simulations*, JHEP **07** (2014) 079, [arXiv:1405.0301].

[101] K. Cheung, J. S. Lee, and P.-Y. Tseng, *New Emerging Results in Higgs Precision Analysis Updates 2018 after Establishment of Third-Generation Yukawa Couplings*, JHEP **09** (2019) 098, [arXiv:1810.02521].

[102] S. Y. Choi, J. S. Lee, and J. Park, *Decays of Higgs bosons in the Standard Model and beyond*, Prog. Part. Nucl. Phys. **120** (2021) 103880, [arXiv:2101.12435].

[103] Y. Tan et al., *Search for invisible decays of the Higgs boson produced at the CEPC*, Chin. Phys. C **44** (2020), no. 12 123001, [arXiv:2001.05912].

[104] M. Quiros, *Finite temperature field theory and phase transitions*, 1999.

[105] M. Quiros, *Finite temperature field theory and phase transitions*, in ICTP Summer School in High-Energy Physics and Cosmology, pp. 187–259, 1, 1999. hep-ph/9901312.

[106] C. L. Wainwright, *CosmoTransitions: Computing Cosmological Phase Transition Temperatures and Bubble Profiles with Multiple Fields*, Comput. Phys. Commun. **183** (2012) 2006–2013, [arXiv:1109.4189].

[107] M. Hindmarsh, S. J. Huber, K. Rummukainen, and D. J. Weir, *Numerical simulations of acoustically generated gravitational waves at a first order phase transition*, Physical Review D **92** (Dec., 2015).

[108] M. Hindmarsh, S. J. Huber, K. Rummukainen, and D. J. Weir, *Gravitational waves from the sound of a first order phase transition*, Physical Review Letters **112** (Jan., 2014).

[109] J. R. Espinosa, T. Konstandin, J. M. No, and G. Servant, *Energy budget of cosmological first-order phase transitions*, Journal of Cosmology and Astroparticle Physics **2010** (June, 2010) 028–028.

[110] C. Caprini, R. Durrer, and G. Servant, *The stochastic gravitational wave background from turbulence and magnetic fields generated by a first-order phase transition*, JCAP **12** (2009) 024, [arXiv:0909.0622].

[111] P. Binetruy, A. Bohe, C. Caprini, and J.-F. Dufaux, *Cosmological Backgrounds of Gravitational Waves and eLISA/NGO: Phase Transitions, Cosmic Strings and Other Sources*, JCAP **06** (2012) 027, [arXiv:1201.0983].

[112] C. Caprini, M. Hindmarsh, S. Huber, T. Konstandin, J. Kozaczuk, G. Nardini, J. M. No, A. Petiteau, P. Schwaller, G. Servant, and D. J. Weir, *Science with the space-based interferometer elisa. ii: gravitational waves from cosmological phase transitions*, Journal of Cosmology and Astroparticle Physics **2016** (Apr., 2016) 001–001.

[113] S. Kawamura et al., *Current status of space gravitational wave antenna DECIGO and B-DECIGO*, PTEP **2021** (2021), no. 5 05A105, [arXiv:2006.13545].

[114] **LISA** Collaboration, P. Amaro-Seoane et al., *Laser Interferometer Space Antenna*, arXiv:1702.00786.

[115] G. M. Harry, P. Fritschel, D. A. Shaddock, W. Folkner, and E. S. Phinney, *Laser interferometry for the big bang observer*, Class. Quant. Grav. **23** (2006) 4887–4894. [Erratum: Class.Quant.Grav. 23, 7361 (2006)].

[116] W.-R. Hu and Y.-L. Wu, *The Taiji Program in Space for gravitational wave physics and the nature of gravity*, Natl. Sci. Rev. **4** (2017), no. 5 685–686.

[117] Z. Luo, Z. Guo, G. Jin, Y. Wu, and W. Hu, *A brief analysis to Taiji: Science and technology*, Results Phys. **16** (2020) 102918.

[118] Z. Luo, Y. Wang, Y. Wu, W. Hu, and G. Jin, *The Taiji program: A concise overview*, PTEP **2021** (2021), no. 5 05A108.

[119] **TianQin** Collaboration, J. Luo et al., *TianQin: a space-borne gravitational wave detector*, Class. Quant. Grav. **33** (2016), no. 3 035010, [arXiv:1512.02076].

[120] **CMS** Collaboration, *Technical proposal for a MIP timing detector in the CMS experiment Phase 2 upgrade*, tech. rep., CERN, Geneva, 2017.

[121] D. Contardo, M. Klute, J. Mans, L. Silvestris, and J. Butler, *Technical Proposal for the Phase-II Upgrade of the CMS Detector*, tech. rep., Geneva, 2015. Upgrade Project Leader Deputies: Lucia Silvestris (INFN-Bari), Jeremy Mans (University of Minnesota) Additional contacts: Lucia.Silvestris@cern.ch, Jeremy.Mans@cern.ch.

[122] C. Allaire et al., *Beam test measurements of Low Gain Avalanche Detector single pads and arrays for the ATLAS High Granularity Timing Detector*, JINST **13** (2018), no. 06 P06017, [arXiv:1804.00622].

[123] **LHCb** Collaboration, R. Aaij et al., *Physics case for an LHCb Upgrade II - Opportunities in flavour physics, and beyond, in the HL-LHC era*, arXiv:1808.08865.

[124] J. Liu, Z. Liu, and L.-T. Wang, *Enhancing Long-Lived Particles Searches at the LHC with Precision Timing Information*, Phys. Rev. Lett. **122** (2019), no. 13 131801, [arXiv:1805.05957].

[125] **CMS** Collaboration, V. Khachatryan et al., *Search for dark matter, extra dimensions, and unparticles in monojet events in proton–proton collisions at* $\sqrt{s} = 8$ *TeV*, Eur. Phys. J. C **75** (2015), no. 5 235, [arXiv:1408.3583].

[126] E. Bartz et al., *FPGA-Based Tracklet Approach to Level-1 Track Finding at CMS for the HL-LHC*, EPJ Web Conf. **150** (2017) 00016, [arXiv:1706.09225].

[127] **CMS** Collaboration, *Muon ID performance: low-p_T muon efficiencies*, .

[128] A. Alloul, N. D. Christensen, C. Degrande, C. Duhr, and B. Fuks, *FeynRules 2.0 - A complete toolbox for tree-level phenomenology*, Comput. Phys. Commun. **185** (2014) 2250–2300, [arXiv:1310.1921].